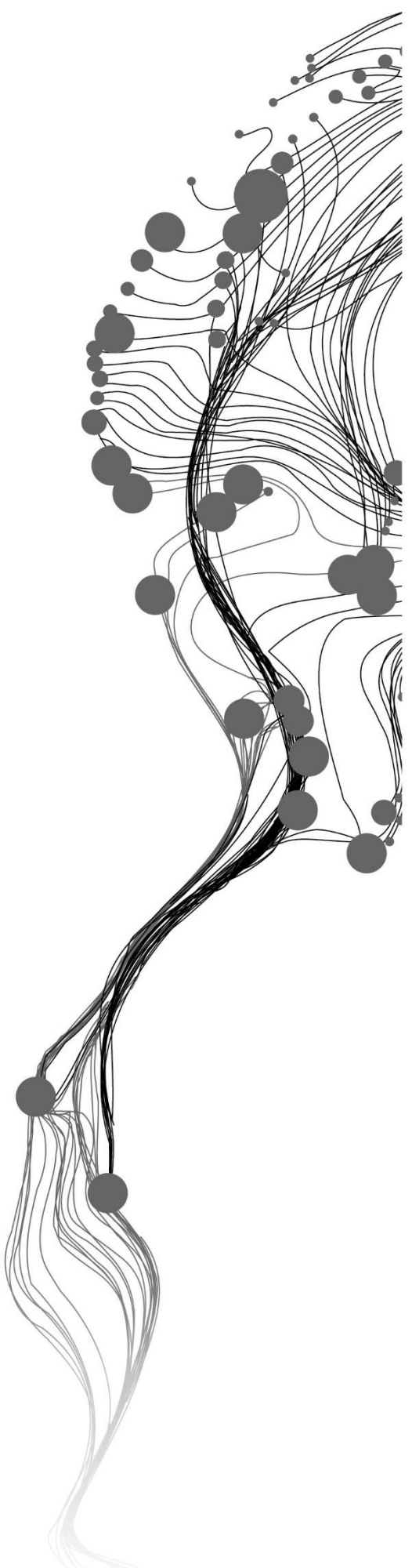


**MONITORING THE ACTIVITIES OF
FUMARoles USING THERMAL INFRARED,
METEOROLOGICAL, AND GAS CHEMISTRY
DATA IN THE OLKARIA GEOTHERMAL
FIELD: A POSSIBLE LINK TO THE
GEOTHERMAL MOTOR?**

BENARD MAGETO OMWENGA
August, 2021

SUPERVISORS:
Dr. C.A. Hecker
Dr. H.M.A. van der Werff



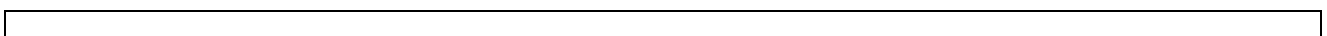
MONITORING THE ACTIVITIES OF FUMARoles USING THERMAL INFRARED, METEOROLOGICAL, AND GAS CHEMISTRY DATA IN THE OLKARIA GEOTHERMAL FIELD: A POSSIBLE LINK TO THE GEOTHERMAL MOTOR?

BENARD MAGETO OMWENGA
Enschede, The Netherlands, August, 2021

Thesis submitted to the Faculty of Geo-Information Science and Earth Observation of the University of Twente in partial fulfilment of the requirements for the degree of Master of Science in Geo-information Science and Earth Observation.
Specialization: Applied Remote Sensing for Earth Sciences

SUPERVISORS:
Dr. C.A. Hecker
Dr. H.M.A. van der Werff

THESIS ASSESSMENT BOARD:
Prof. dr. M. van der Meijde (Chair)
Dr. T.A. Groen (External examiner)



DISCLAIMER

This document describes work undertaken as part of a programme of study at the Faculty of Geo-Information Science and Earth Observation of the University of Twente. All views and opinions expressed therein remain the sole responsibility of the author, and do not necessarily represent those of the Faculty.

ABSTRACT

Long-term monitoring of fumarole temperatures variation can provide insight into the subsurface behavior, especially fluxes in the geothermal and volcanic system. Conventional field-based monitoring methods, e.g., calorimetric methods, though accurate, are limited in the temporal frequency domain. The thermal infrared data, especially geostationary thermal infrared sensors' have widely been useful for fumarole monitoring, especially in eruptive volcanic surveillance studies. However, pertinent issues such as spatial resolution and influences of atmospheric and surface effects on recorded temperature values have hampered comprehensive monitoring campaigns. For this reason, the study investigated the activities of fumarole in line with the following objectives: (i) apply high temporal resolution thermal infrared imagery to study surface temperature variation as a proxy to subsurface geothermal heat flux, (ii) To understand external factors affecting the apparent temperature using weather data (air temperature and precipitation), (iii) contextualize subsurface dynamics of the geothermal reservoir using fumarole gas discharge data.

Data processing was done procedurally: Demarcation of regions of interest from specific hour-of-day TIR imagery by visual inspection of principal component analysis, temporal mean, standard deviation, and optical image collected by the daytime timelapse camera. Secondly, time series plots of the apparent radiant temperature of the demarcated regions of interest were generated and their long-term patterns analysed. The third step involved removing low-quality images based on the standard deviation value of pixels of time series TIR images. Normalization of time series plots was done to remove further daily components associated with environmental effects. Finally, the normalized time series plots were used to calculate radiative heat flux plots. Finally, fumarole gas concentration data were plotted, and temporal patterns were analysed.

The results show comparable spatial patterns within indicator products of principal component analysis, temporal mean products of selected hour-of-day TIR images. The temporal of time series plots of different ROIs extracted from TIR show variation with seasonality. The variations were related to existing environmental conditions and were specifically enhanced during rainy periods. The periodicity also varied per region of interest and was optimal in thermally anomalous sections near the fumarole area. The results further show that removing images acquired during foggy conditions and the time normalization procedure eliminated anomalous signals from time series plots. The heat flux plots, calculated from normalized radiant temperature values, were useful in identifying endogenous processes associated with subsurface heat emission. Finally, fumarole gas chemistry concentration plots show variability with occasional peaks (between July 2008 to June 2020), which were attributed to subsurface processes such as dilution and boiling. Such processes were linked with the variability of subsurface fluid movement, an aspect of fluctuating speeds of the geothermal motor.

In conclusion, the study revealed that TIR imagery acquired by ground-based thermal infrared cameras is a useful tool in monitoring fumarole's thermal behavior in a productive geothermal field. Besides, the study's novelty lies in isolating external influences from TIR infrared imagery time series data, analyzing the residual trends, and associating them with subsurface geothermal activities.

Key words: Fumarole monitoring, Thermal Infrared time series, gas chemistry, Geothermal motor

ACKNOWLEDGEMENTS

I wish to thank my employer, Kenya Electricity Generation Company, PLC, for permitting me to pursue the MSc studies. I also thank them for sponsoring my studies for the entire period of study. Special mention to Eunice Bonyo and the entire KenGen team for availing of the data used in this study. Special thanks to my office supervisors and other colleagues for their support during my study period

I also would like to express my gratitude to my supervisors, Dr. Chris Hecker and Dr. Harald van der Werff, for their unwavering support during the research period. I thank them for guidance and patience during the data analysis and interpretation phases. In addition, instilled a culture of hard work and critical thinking that has positively impacted my academic scope.

I'm also grateful to the chair, Prof Mark van der Meidje, for the proposal and mid-term presentation suggestions. Special thanks to the academic staff of the Earth system Analysis (ESA) for providing useful courses that were helpful in the execution of this thesis.

Finally, I wish to thank my family for being there for me throughout the academic period.

TABLE OF CONTENTS

1.	INTRODUCTION	6
1.1.	Background.....	6
1.2.	Fumarole monitoring in geothermal systems	7
1.3.	Problem statement	8
1.4.	Research Objectives	9
1.5.	Study Area.....	10
2.	DATASETS AND METHODS	13
2.1.	Datasets.....	13
2.2.	Data processing.....	18
2.3.	Geothermal heat flux estimation	24
2.4.	Analysis of gas discharge chemistry data.....	26
3.	RESULTS	27
3.1.	Spatial subsets into regions of interest.....	27
3.2.	Foggy scenes removal.....	35
3.3.	Time series normalization.....	37
3.4.	Geothermal heat flux estimation	37
3.5.	Analysis of gas discharge chemistry data.....	38
4.	DISCUSSION	40
4.1.	Discussion of spatial subset into ROIs.....	40
4.2.	Discussion of fog removal thresholding algorithm	41
4.3.	Discussion of time series normalization.....	42
4.4.	Discussion of heat flux estimation and implications on the geothermal motor	42
4.5.	Discussion of gas geochemistry	43
4.6.	Limitations of the study	44
5.	CONCLUSIONS AND RECOMMENDATIONS.....	46
5.1.	Conclusions	46
5.2.	Recommendations.....	47
6.	APPENDICES.....	52

LIST OF FIGURES

Figure 1.1: The study area and its location among other geothermal fields..	10
Figure 1.2: Distribution of geological structures in the study area.....	11
Figure 2.1: Installation of field lab station at the Olkaria Geothermal Field.....	14
Figure 2.2: Field sampling of OMF8 at the Olkaria Geothermal Field.....	16
Figure 2.3: A sketch of equipments used for sampling of fumarole gas	16
Figure 2.4: Methodological workflow	19
Figure 2.5: Schematic flow chart showing steps in ROI creation	21
Figure 2.6: Background removal normalization procedure	24
Figure 2.7: Estimated distance between thermal camera and OMF8.	26
Figure 3.1: Principal Component Analysis and time lapse camera images	27
Figure 3.2: Temporal mean and time lapse camera images	28
Figure 3.3: Temporal standard deviation and time lapse images	30
Figure 3.4: Variation of apparent temperature values of ROI-4.	31
Figure 3.5 : Variation of apparent temperature values of ROI-3.	32
Figure 3.6: Variation of apparent temperature values of ROI-2.	33
Figure 3.7: Variation of apparent temperature values of ROI-1	34
Figure 3.8: Time series plots of fog removed scenes.....	36
Figure 3.9: Normalized time series plots	37
Figure 3.10: Heat flux plots	38
Figure 3.11: (A) Temporal variation of CO ₂ , H ₂ S between and chloride.....	39

LIST OF TABLES

Table 1: Technical specification of the thermal infrared camera at OMF8.....	13
Table 2: Selected elements and gases used for the for fumarole activity monitoring	17
Table 3: Confusion matrix to assess fog removal algorithm’s performance.....	22
Table 4: Measured radiant temperature of different ROIs.....	29
Table 5 Standard deviation distribution across different ROIs of selected hour-of-day.....	30
Table 6: Summary of TIR scenes flagged by algorithm	35
Table 7: Confusion matrix showing performance of algorithm on 00:00 UTC TIR scenes.....	36
Table 8: Table 3.4: Confusion matrix showing performance of algorithm on 09:00 UTC TIR scenes.....	36

1. INTRODUCTION

1.1. Background

Geothermal energy is the heat that emanates from the earth's surface (Meyers, 2012). The energy is formed by heat flow from the earth's core as a result of the decaying of radioactive elements such as K, Th, and U (Lund, 2013). Exploitable geothermal energy resources are found in various geological environments, predominantly along high crustal heat zones and active volcanic systems (Haselwimmer et al., 2013). The energy resource is often characterized by surface manifestation features such as fumaroles, hot springs, mud pools, and volcanic centers. Globally, many geothermal systems have been exploited for power generation. Among them are those in the East African Rift System (EARS), with an estimated potential capacity of over 10000 Megawatts electric (MWe) (Omenda, 2018). Within this system is the Greater Olkaria Geothermal Area (GOGA), which has been extensively exploited for electric power generation and is the focus of this study (elaborately described in section 1.5).

To generate geothermal electricity, production wells are drilled to extract fluids or steam to spin geothermal powerplant turbines. Also, separated brine and power plant condensate are reinjected into the reservoir to ensure resource recovery and sustainability (Diaz et al., 2016). If the extraction of geothermal reservoir fluids exceeds the rate of reinjection, mass imbalance of the geothermal system might occur (Fadel et al., 2021). Mass imbalance is occasionally characterized by changes in the geothermal systems, such as unusual compositional variation in fumarole gas, the collapse of earth materials along highly altered surfaces (Malvina et al., 2019), and increased seismic activity (Rashmin et al., 2003). In extreme cases, it is characterized by a decline and eventual extinction of surface manifestation features (Barrick, 2007), a phenomenon experienced in the Rotorua geothermal field, New Zealand (Hunt, 2013). Therefore, there is a need to monitor and understand geothermal systems' activities and their relationship with the 'geothermal motor'.

The term 'geothermal motor' was recently introduced by Fadel et al. (2021). They defined it as the movement of large convective cells within a geothermal reservoir that distribute hot and cold fluids along up flow and downflow zones in a geothermal system. Also, the description by Reinsch et al. (2017) in p.12, 'the dynamics of hydrothermal fluids in the earth's subsurface that characterizes the geothermal reservoir,' gives an alternative overview of the concept. Hot fluids originating from the reservoir rocks are circulated upwards while cool meteoric fluids from direct precipitation recharge flows downwards in a 'motor-like' pattern.

Generally, the activities of the geothermal motor significantly affect the sustainability of the geothermal resource. An imbalance in the geothermal system causes unintended changes in the speed and efficiency of the geothermal motor. Such changes can be detected by long-term monitoring surface and subsurface changes of a geothermal

reservoir. The long-term monitoring of reservoir pressures/ temperatures and heat flux changes of surface manifestation features (e.g., fumaroles), guides in understanding a geothermal motor's behavior. As such, it is necessary to adopt a comprehensive monitoring plan to ensure sustainable utilization of the resource and avert future problems associated with increased exploitation of the geothermal resource (Axelsson, 2010). The behavior of surface manifestations features such as fumaroles offers a glimpse into the status of a geothermal reservoir which can indirectly link to the geothermal motor behavior.

1.2. Fumarole monitoring in geothermal systems

Fumaroles are important surface manifestation expressions associated with convective geothermal reservoirs. They are found in high and moderate-temperature geothermal systems, with characteristic reservoir temperatures of over 200 °C and fluid enthalpies in excess of 800 kJ/kg (Axelsson, 2010). By observing the thermal hydrothermal fluids and steam emitted by fumaroles, it is possible to understand the state of fluids within the geothermal system (Inguaggiato et al., 2018). Similarly, periodic variation of fumarole gas composition (i.e., CO₂, CH₄, H₂, and N₂) cannot at all give insight into degassing activities, often associated with changes in pressure and temperatures of fluids in the geothermal reservoirs (Hunt, 2013). Also, quantifying and monitoring long-term fluctuation of surface parameters such as radiative heat flux and discriminating the meteorological components makes it possible to understand the processes within a geothermal system (Malvina et al., 2019).

For many years, conventional field-based methods such as calorimetric monitoring (Ozawa, 1958), chloride-inventories (Ingebritsen & Mariner, 2010), soil-temperature (Dawson & Dickinson, 1970), and fumarole gas flux (Wen et al., 2016) methods have been used to monitor fumarole behavior in geothermal fields. Usually, a network of thermal probes and funnel flasks are inserted within fumarole vents to measure kinetic temperature and gas composition. These methods are relatively cheap, comparatively sensitive, and reflect actual in-situ conditions (Gaudin et al., 2017; Malvina et al., 2019). However, there are also notable weaknesses in the aforementioned methods. Firstly, calorimetric measurements are not suitable for monitoring high-temperature fields (Lindsey et al., 2015). Secondly, temperature and gas flux measurements are affected by inaccuracies arising from sampling and instrument calibration (Coolbaugh & Sladek, 2013). Moreover, the field-based methods do not provide a synoptic view of the spatial distribution of the surface heat variation. There are chances of overestimation as a result of focusing on a subset of the area of interest (Gaudin et al., 2017). Consequently, some gaps may arise inconsistent temporal resolution of the data. Thermal infrared remote sensing is considered a viable alternative.

Time-series data derived from sun-synchronous orbit thermal infrared remote sensors (e.g., ASTER, Landsat ETM+) have gained extensive usage in monitoring the thermal variation of geothermal fields (Chan & Chang, 2018; Haselwimmer et al., 2013; Mia, Bromley, & Fujimitsu, 2012). Anomalous signals trends arising from Land Surface temperature(LST), surface latent heat flux, or top-of-the atmosphere long wave radiance derived from these sensors are used to characterize geothermal fields on a low spatial and temporal resolution context (Malvina

et al., 2019; Mia et al., 2012; Vaughan et al., 2012). Although such datasets address some gaps associated with field-based methods (e.g., low synoptic coverage), they are affected by topographical and terrain differences and localized weather conditions such as winds and cloud cover (Kuenzer & Dech, 2013). Thus, subtle signal anomalies related to physical processes associated with geothermal motor/system activities might go unnoticed.

To address this shortcoming, high temporal resolution ground-based thermal infrared cameras have been adopted for indirect geothermal monitoring (Silvestri et al., 2020). They record radiated heat and quantify them into temperature measurements, visualized as thermal images (Kuenzer & Dech, 2013). The radiant temperature values are subsequently used for the estimation of surface radiative heat flux, which can give insight into the subsurface behavior of the reservoir systems. Their usage in geothermal investigations has been limited to hot water geothermal systems (Haselwimmer et al., 2013). In this case, the usage has been confined to quantification of heat flux and estimation of flow rates of geothermal springs. Other applications have mostly been used to detect and monitor thermal anomalies that might trigger eruptions of quiescent volcanoes (Chiodini et al., 2007; Sansivero & Vilardo, 2019; Stevenson & Varley, 2008).

1.3. Problem statement

One way to qualitatively monitor a geothermal system's activities is by assessing the surface temperature variation at specific geothermal hotspots (fumarole) on a multi-temporal basis (Stevenson & Varley, 2008). By examining the daily or seasonal variation of surface radiant temperature time series trends, it is possible to identify outlier signals which can be linked shallow and deep subsurface hydrothermal processes (e.g., magma degassing). However, Sansivero & Vilardo (2019) showed that such signals may be associated with other external influences that are both of atmospheric (e.g., precipitation, fog, solar illumination) and surface (emissivity, differential thermal inertia) origin. Efforts have been made to detect and isolate these artifacts, using a variety of time series detrending techniques. For instance, Chiodini et al., (2007), and Sansivero et al., (2013) applied the background removal techniques to isolate these artifacts and use the residual values to identify signals linked with mild explosions in volcanic systems. However, these findings were still inhibited by fog and precipitation, resulting in more false signals that were specifically enhanced on predawn TIR imagery acquired during rainy and foggy weather conditions. In addition, the lower temporal frequency of data used (i.e., weekly interval) meant that higher number of flagged scenes, thereby compromising the eventual residual trends.

Bearing the above mentioned limitations, this study, tested the detrending technique on similar datasets using higher temporal acquisition rate (hourly interval) in a productive geothermal field. In addition, the technique was also tested on day-time TIR scenes to check whether such influences can be minimized by using different day-time images. The resulting residual temperature was then integrated with subsurface data (i.e., fumarole gas chemistry) to understand subsurface variability; and link them with the 'geothermal motor.'

1.4. Research Objectives

1.4.1. Overall objective

To investigate the applicability of high temporal resolution time series of ground-based thermal infrared scenes, combined with fumarole gas concentration and meteorological time series data, as a monitoring tool for fumarole activity of the Olkaria productive geothermal system.

1.4.2. Specific objectives

Objective 1

To define and isolate potential external (surface and atmospheric) influences on recorded radiant temperature.

- ❖ Which indicators can be used to define and isolate these influences? How do they spatially change over different hours of the day?
- ❖ How do the minimum, maximum, and mean values of radiant temperature from specific zones of TIR images vary in time? How do they relate with the time series plots of meteorological parameters?

Objective 2

To perform a correction to remove potential outlier signals associated with external influences.

- ❖ Which pixel indicators can be used to isolate these signals? How effective are the indicators under different atmospheric conditions over different hours of acquisition?

Objective 3

To analyse the temporal variation of the temperature corrected for external influences.

- ❖ Is there a notable trend in the time series temperature plots? If so, what is their general temporal behavior?
- ❖ How does the periodicity of the apparent radiant temperature trends relate to the daily weather trends?

Objective 4

To ascertain whether there exist a relationship between the surface heat flux (calculated from corrected detrended surface radiant temperature) and fumarole gas composition data.

- ❖ What are the general trends of the heat flux and gas chemistry time series plots? Are there any outlier signals? If so, how does this link to the speed of the geothermal motor?

The structures also act as conduits or flow paths for surface fluids (Ofwona, 2002). Axelsson et al., (2013) further states that cold fluids (of meteoric origin) infiltrate into the geothermal system through N-S fault systems along the Ololbutot fault axis, which is characterized by numerous fumaroles. This is specifically interesting for this study because (OMF8), the fumarole of focus, is situated along the Ololbutot lava flow flanked by the numerous fault systems (see Figure 1.2).

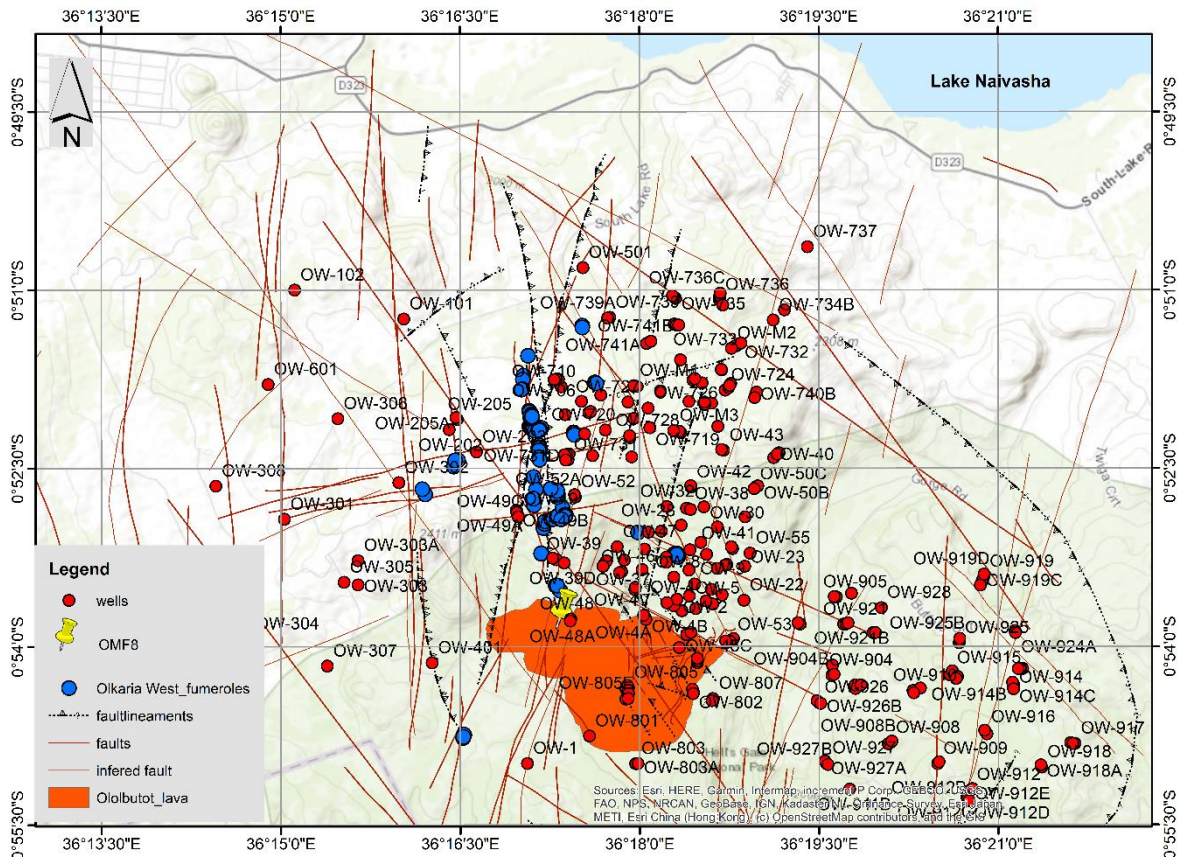


Figure 1.2: Distribution of various geological structures and surface geothermal manifestations in the study area (Topographic background map sourced from ESRI (2021), while shapefiles are sourced from KenGen, PLC database). Note the N-S alignment of fumaroles (blue dots), an indication of structural control. The yellow pointer shows the position of fumarole of study.

1.5.3. Status of Geothermal exploitation of the study area

The Olkaria geothermal field area has been exploited for geothermal power since the 1980s. Recently, the field has witnessed increased exploitation of geothermal resources for power generation. Notable developments include the recent commissioning of the 280 Mwe powerplants in 2015 (Njoroge, 2016). Over the past years, some reservoir-induced changes have been observed, with the most notable being moderate well pressure decline and fluid chemical changes in some selected wells within the field (Ouma et al., 2016). For instance, the drop in chloride levels of geothermal wells OW-15, OW-16, and OW-18, was recorded between 1995 to 2017, was attributed to reinjection in the field (Wafula, 2018) to stabilize the field’s pressure drawdown..

Other wells such as OW-05, OW-15, OW-18, OW-19, OW-20 in the East field have also shown high enthalpy changes (Koech, 2014). During this period, the chloride, CH₄, and CO₂ of fluid condensate, significantly increased, a phenomenon attributed to increased subsurface boiling processes (Karingithi, 2015). Importantly, these wells sited near the Olobutot fault axis, which acts as hydrological barrier, controlling inflow of surface recharge into the system (Axelsson et al., 2013). In addition, OMF8 which is the focus of this study, is located in this zone thus changes might give an idea of the subsurface processes affecting the system.. Consequently, monitoring plans have been placed to observe the geothermal system's response.

2. DATASETS AND METHODS

2.1. Datasets

2.1.1. Thermal infrared imagery

These were the primary datasets for this study. The datasets comprised of thermal infrared (TIR) images were acquired using ground-based broadband FLIR A6555sc thermal cameras. Two identical cameras with different lenses were installed on two fumaroles, i.e., OMF8, located at the Ololbutot lava flow (Figure 2.1-A), and OMF6 sited along the Olnjorowa Gorge (Figure 2.1-B) in the Olkaria geothermal field, Kenya. The cameras are sensitive in the longwave infrared wavelength range between 7.5-14 μm (FLIR, 2021). Both cameras collected data between 19th July 2019 to 24th March 2021 at an hourly interval. However, occasional breaks in power supply meant that data gaps were encountered during the acquisition periods. This study deals with data collected at OMF8.

The detailed specifications of the camera at OMF8 are shown in

Table 1. Some of the camera's parameters were used in the estimation of radiative heat flux in section 2.3.

The radiant temperatures recorded by the thermal infrared camera are apparent for each pixel in object space. The temperatures are recorded in Kelvin*10 and converted to Degree Celsius in ENVITM software. A sample image acquired by thermal camera at OMF8 is shown in Figure 2.1-D.

Table 1: Technical specification of the thermal infrared camera at OMF8 (FLIR, 2021)

Field of view	45° × 34°
Lens focal length (mm)	13.1
Spatial pixels (length × width)	640 × 480 pixels
Image size (length × width)	73 × 75 mm
Approximate distance between camera to target (m)	20m
Size [L x W x H] of Lens	216 × 73 × 75 mm
Detector type	Uncooled Microbolometer
Temperature range	-40°C to 650°C

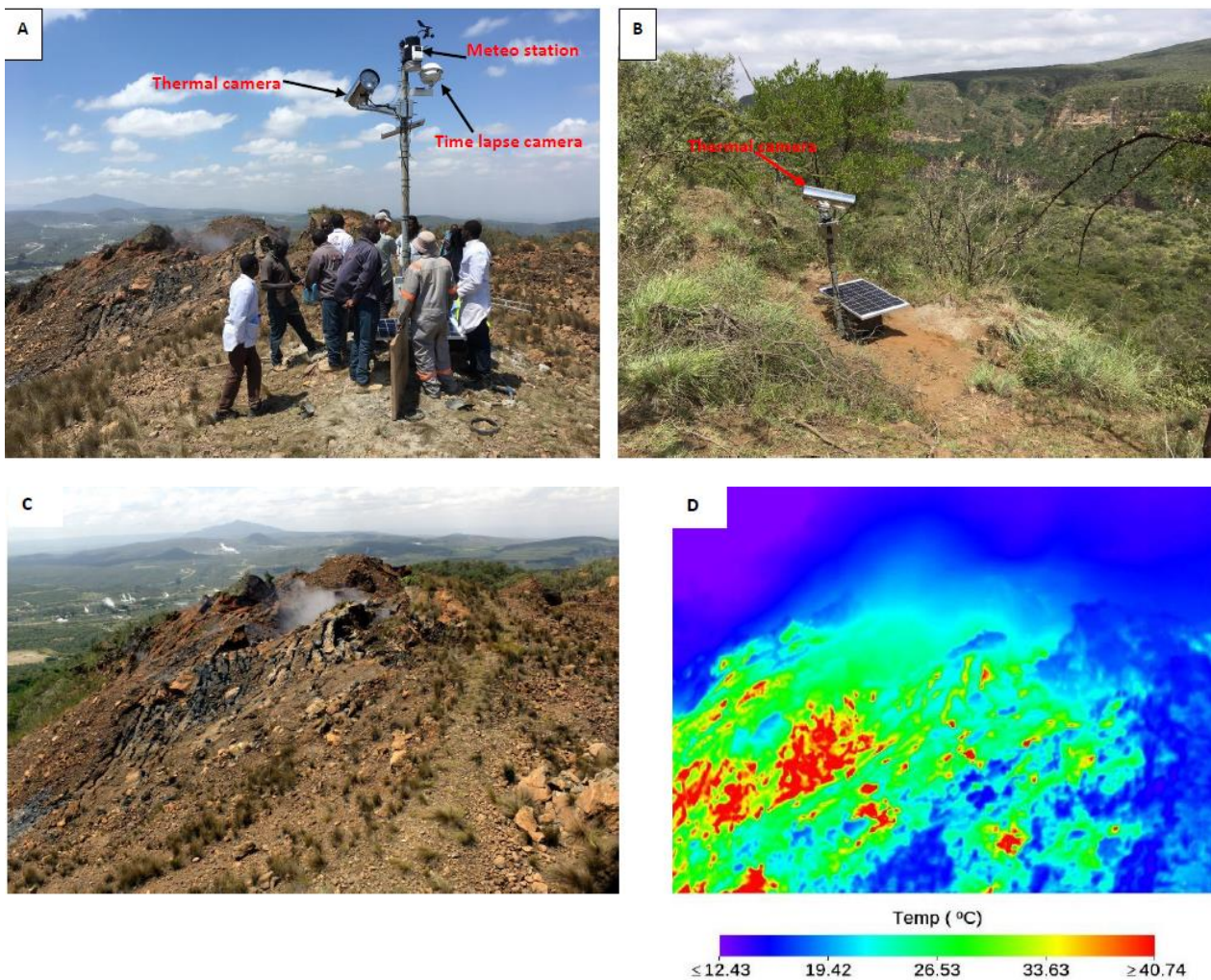


Figure 2.1: A) Installation of field lab station with a thermal camera, time-lapse camera, and meteorological station at OMF8. B) Thermal infrared camera at OMF6. C) A daytime optical image of OMF8 acquired by a time-lapse camera. D) Sample thermal infrared image, acquired at OMF8; the warmer pixels are located near the fumarole vent, while the sky and background regions are cooler.

2.1.2. Time-lapse camera imagery

The time-lapse imagery are RGB images acquired by a time-lapse camera installed with the thermal camera at the OMF8 in the Ololbutot lava flow (Figure 2.1-A). The camera records two images per day, one acquired at local noon and another in the late evening. The noon acquisition aims to monitor surface variation under maximum solar angle and illumination. The late afternoon images are useful in monitoring the surface conditions under maximum contrast conditions.

The time-lapse camera imageries were primarily purposed to investigate the surface movements around the main fumarole area. However, in this study, they were combined with other TIR image products to demarcate different land cover for further spatial and temporal analysis (see section 2.2.2 for elaborate explanation).

2.1.3. Meteorological parameters

Meteorological data was recorded by a "Davis Vantage Pro" meteorological station installed with the OMF8 thermal camera at the Ololbutot lava flow (Figure 1.1A). The recorded parameters include rainfall, air temperature, wind speed, barometric pressure, relative humidity, solar irradiance, and soil moisture. The data sets were helpful in monitoring and understanding surface-atmospheric interactions, which affect apparent radiant temperatures recorded by thermal infrared cameras. For this study, precipitation and air temperature data have been used.

The data acquisition began on 19th July 2019 at an hourly interval and was ongoing at the time of this report's preparation. Therefore, for this study, only data acquired between 19th July 2019-24th December 2020 has been used. A data gap was observed between 4th December 2019-1st January 2020 and 7th June to 1st July 2020.

2.1.4. Fumarole gas chemistry data

Sampling of fumarole gas discharge and laboratory analysis of its chemical constituents was carried out by a team from the Kenya Electricity Generation Company, PLC (see Figure 2.2) based on the method proposed by Arnórsson et al. (2006) as follows:

- i. Insertion of stainless steel funnel tube into the fumarole vent. The funnel's contact with the steam vent was sealed with mud to avoid possible contamination with air.
- ii. Gases were then directed into an evacuated (giggenbach) flask containing about 50 ml of 40% NaOH solution to trap non-condensable gases. The flask was immersed in a bucket of water e to push the condensate through the tube.
- iii. The acidic gases (e.g., CO₂ and H₂S) are dissolved into the NaOH solution. The non-acidic gas species (e.g., hydrogen (H₂), methane (CH₄), nitrogen (N₂), and oxygen (O₂)) are determined using the gas chromatography technique. Other condensate samples are used for the analysis of volatiles. A portion of the condensate is also set aside for in-situ measurements, e.g., pH, Total Dissolved Solids (TDS), among others.

The above-mentioned processes are shown in a sketch in Figure 2.3.

The sampling was carried out on a 3-month basis, from 27th July 2019 to 18th March 2021. Archived data recorded from 4th February 2018 was incorporated to have a historical overview of the compositional changes of the gases. However, the sampling frequency was irregularly done (approximately after 3 months) due to logistical challenges.

For this study, three constituents, namely: carbon dioxide (CO₂), Hydrogen dioxide (H₂S), and chloride (Cl) have been analysed and interpreted (See Table 2 for further clarification).



Figure 2.2: Field sampling of OMF8 at the Olkaria Geothermal Field (Source: KenGen internal database)

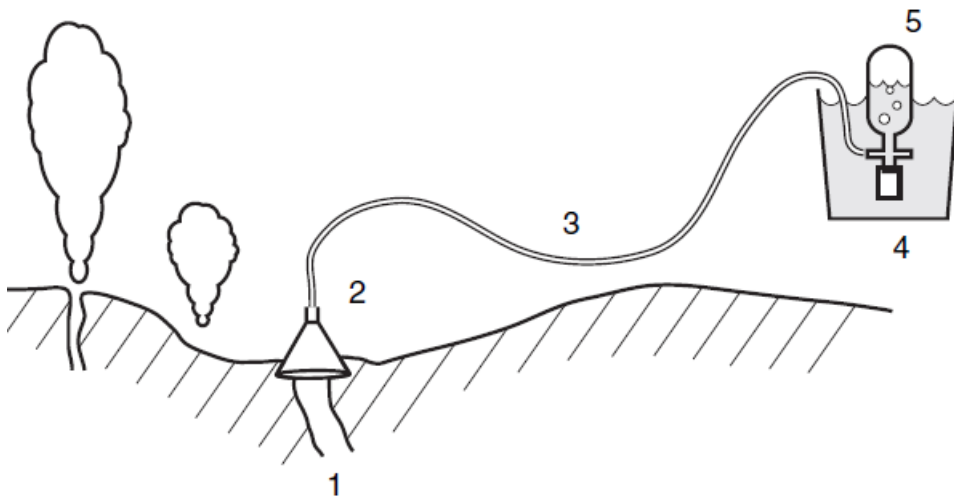


Figure 2.3: A sketch of equipments used for sampling of fumarole gas discharge (Arnórsson et al., 2006). (1) Fumarole steam outlet, (2) Funnel, (3) silicon tubing (4). Bucket with cold water to cooling the condensate (5). evacuated (Giggenbach) flask

Table 2: Selected elements and gases used for the for fumarole activity monitoring

Element/compound	Reason for selection
CO ₂ and H ₂ S	<ul style="list-style-type: none"> • They are most dominant gas species of a geothermal system. The increase or decrease of these parameters reflects magmatic degassing activities in a geothermal system (Hunt, 2013). • Increased H₂S is associated with percolation of cool fluids into geothermal reservoir .
Chloride	<ul style="list-style-type: none"> • These element is associated with dilution of shallow thermal waters; and is linked with surface shallow recharge. Their variation of is also linked with reinjection of cold fluids into the geothermal system (Karingithi, 2015).

The time series of the plots of the above-mentioned parameters were created (section 2.4), and subsequent analysis and interpretations made.

2.2. Data processing

This section outlines the various steps involved in the analysis of TIR images and other ancillary datasets used in the study. The data processing procedure was carried out sequentially as follows:

- i. Temporal subset by the hour of acquisition: this involves selecting a specific hour of the daytime series TIR images in order to understand how radiant temperature changes under different environmental and surface conditions (section 2.2.1). This step answers question 1 of the first study objective.
- ii. Spatial subset into regions of interest: This involved demarcating smaller regions of interest from the selective hour-of-day TIR images; to separate areas affected by external influences (i.e., weather, surface material properties) and fumarole activity (proxy to geothermal activities). This step partly answers question 1 of the first objective and question 2 of objective 1. It is described in section 2.2.2.
- iii. Removal of foggy thermal infrared scenes: This step involves removing outlier signals from time series plots of TIR scenes acquired during foggy and rainy weather conditions. The step answers the second objective of the study and is described in section 2.2.3.
- iv. Normalization of the defogged time series data: This step helps explain the findings of objective 2 of the study and involves further exclusion of the dominant daily weather from time series plots resulting from the implementation of step iii. This step is explained in section 2.2.4.
- v. Radiative heat flux estimation: This step involves estimating heat emitted by radiating surface using normalized radiant temperature values (step iv). This answers the fourth objective of the study and has been explained in section 2.3.
- vi. Analysis of fumarole gas chemistry data: This step involves creating and analyzing time series plots of different fumarole gas components. This step also answers the fourth objective of the study.

The above-mentioned data processing steps are presented as a workflow diagram in Figure 2.4.

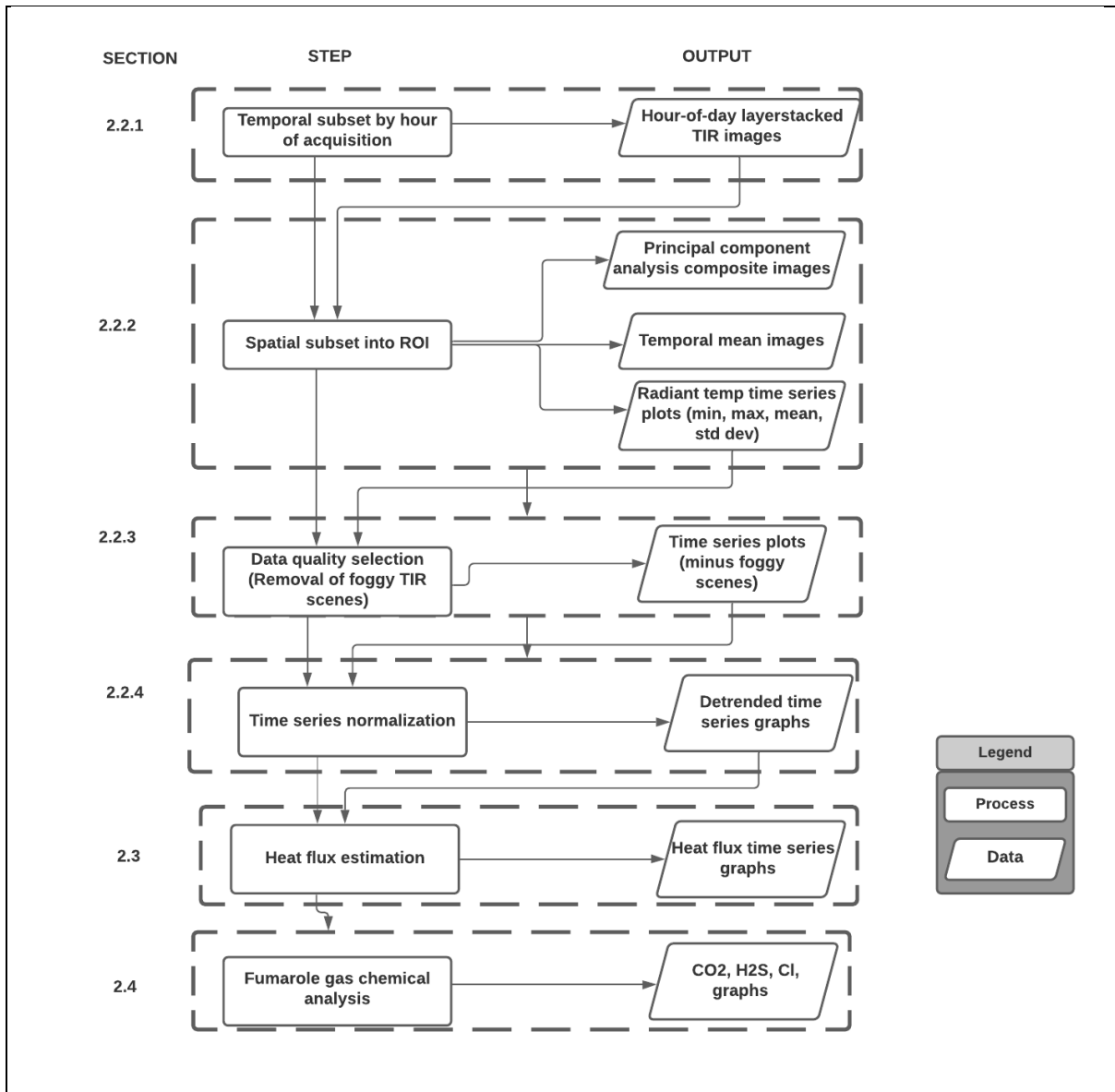


Figure 2.4: Methodological workflow

2.2.1. Temporal subset by the hour of acquisition

This step involved selection of specific hour of day thermal infrared time-series images with the aim of analyzing the spatio-temporal distribution of radiant temperatures under different surface and atmospheric conditions as described below:

- 00:00 and 03:00 UTC (local Predawn and dawn): At this hour of acquisition, the effects of solar illumination are minimal (Romaguera et al., 2018). False anomalies associated with surface albedo, topographic effects, and thermal inertia are minimized.
- 09:00 UTC (local noon): At this time, the sun is overhead, while solar insolation is at its maximum. As such, the radiant temperature values recorded by the TIR camera are relatively high. The surface moisture content is low; therefore, the effects associated with foggy conditions are presumed to be minimal. In addition, effects of thermal shadows on the thermal infrared imagery are minimal.

- 12:00 (Local late afternoon): At this hour, the ground attained maximum heating. Therefore, the soil moisture content is relatively low (higher latent heat loss). Maximum contrast is also observed on the thermal infrared imagery, thus easier to understand the behavior of surface materials based on thermal response to differential solar heating.
- 21:00 UTC (local midnight): At this hour of acquisition, the surface temperatures are relatively low. The surface moisture content is presumably high, while the effects of solar illumination are reduced. It is also possible to identify subtle patterns associated with geothermal influences.

The selection of specific hour-of-day images was made using an ENVI-IDL script, attached in **Appendix 9**

Two hour-of-day time series data with contrasting stability (of radiant temperature values) under different surface and environmental conditions were selected for subsequent Spatio-temporal analysis.

2.2.2. Spatial subsets into regions of interest

Due to the heterogeneity of surface materials in the study area, there was a need to demarcate the image into smaller regions to identify regions affected by external and fumarole (proxy to geothermal influences) activities. Areas affected by fumarole activities are identified in this study as areas with high radiant temperature values consistent over different day hours. On the contrary, background regions are referred to as regions affected by other non-fumarolic factors such as fog, differential heating due to relative slope orientation with regards to solar illumination, among others (Romaguera et al., 2018).

The processes demarcation of specific regions of interest (ROIs) was done chronologically as discussed below:

1. Principal component analysis (PCA) (Lillesand et al., 2008) was performed on selected hour-of-the-day layer stacked TIR images. This was meant to reduce dimensionality and to produce few uncorrelated principal components containing the most information. The first three Principal components containing the most significant percentage of data variance were combined into RGB composite images and used for exploratory analysis. The demarcation was done by interpretation of subtle patterns brought about by contrasting homogeneously colored pixels of PCA composite images.
2. Temporal averaging of radiant temperature and standard deviation values of each pixel in specific hour-of-the-day layerstacked TIR images: For each spatial pixel, the temporal mean and standard deviation was calculated over the whole time-series images. This resulted in two images (temporal mean, standard deviation) that represent the general behavior of each pixel at a certain time of the day. This procedure was done in the ENVI™ software using the ‘*Sum Data Bands*’ function. For this study, these products were used alongside PCA and time-lapse optical images to help identify and demarcate regions of interest for further analysis.
3. Overlay and creation of ROI statistics: The ROIs generated by manually drawing polygons on selected hour-of-day TIR images based on visual comparison with spatial patterns of PCA, temporal mean, standard

deviation, and optical time-lapse camera images. In addition, the statistical parameters (minimum, maximum, mean, and standard deviation) of specific ROIs were extracted and saved as shapefiles for further analysis. Measuring the maximum value in each ROI ensures that the temporal behavior of the hottest pixel was captured. On the other hand, the minimum temperatures ensure that the coldest pixels are captured, while the mean gives an overview of temporal behavior with minimum noise levels for control purposes.

4. Generation of time series plots: Temporal plots of minimum, maximum, mean, and standard deviation of specific ROIs were generated from specific ROIs, then saved as ASCII files for further analysis. Pursuant to objective three of the study, the plots were stacked with meteorological parameters (air temperature, rainfall) to assess their dependence on ambient weather conditions. The stability of time series plots of various ROIs was assessed by visual inspection of synchrony (i.e., the relative distance between line graphs of minimum, maximum, mean). In addition, association with ambient conditions was assessed by correlating minimum radiant temperature values with air temperature values. The time series plots with the highest coefficient of determination are postulated to have the strongest influences of ambient weather conditions (Zimmer et al., 2017).

The above-mentioned steps are shown in Figure 2.5.

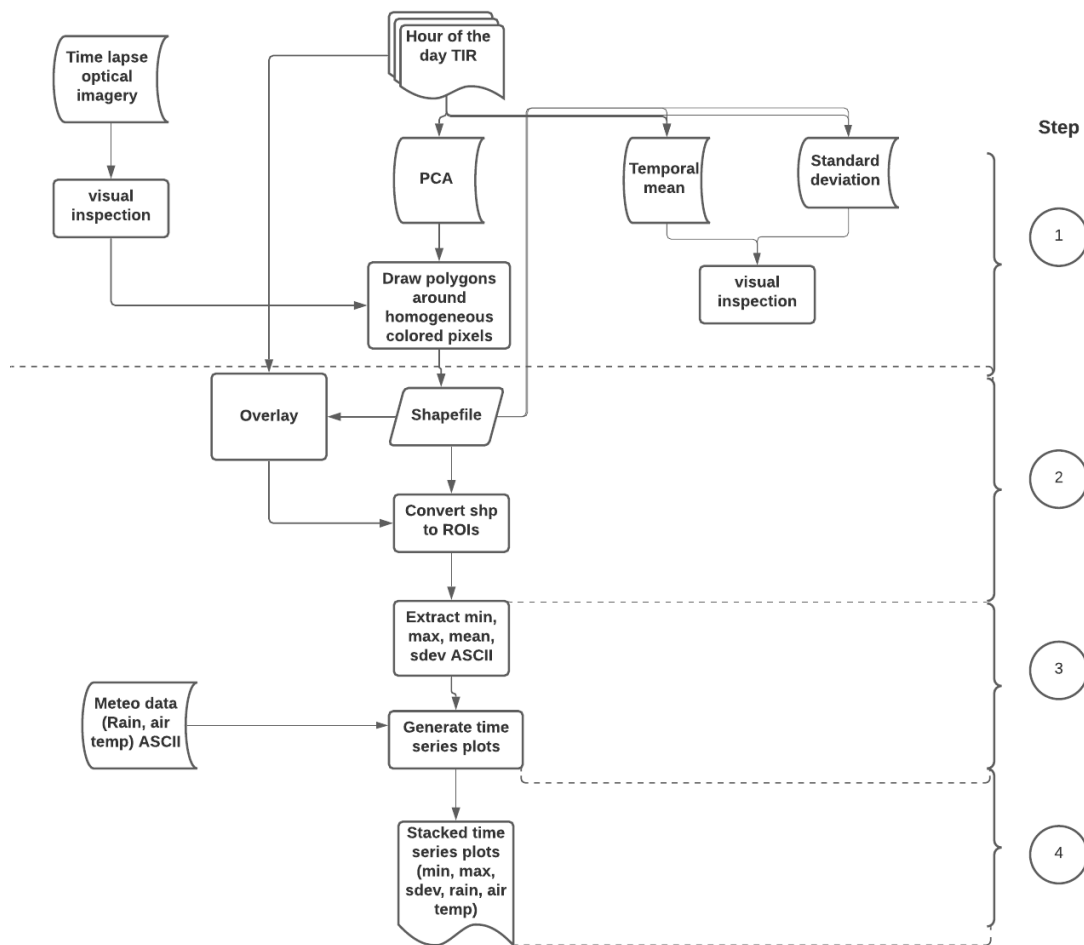


Figure 2.5: Schematic flow chart showing steps in ROI creation

2.2.3. Foggy scenes removal

One of the challenges experienced in processing thermal infrared datasets is the occurrence of hazy images acquired during foggy and rainy weather conditions. Such images are typified by low standard deviation values (i.e., values in lower quantile in a frequency distribution). As such, the thresholding algorithm by Sansivero et al. (2019) was used to isolate the scenes as illustrated in equation (1).

$$\sigma F_i > m\sigma - c * \sigma F_\sigma \quad \text{Equation 1}$$

Where σF_i is the Standard Deviation (SD) of the n^{th} thermal Infrared image, $m\sigma$ is the median of Standard Deviation values of all TIR images, σF_σ is the Standard Deviation of all standard deviations of the thermal infrared scenes, and c is a user-defined coefficient depending on the statistical distribution of data. For this study, the user-defined value of 1 was preferred because it represents values of the lower quartile in a distribution statistical distribution population. The TIR images whose apparent temperature values did not satisfy the condition in equation (1) were excluded.

To evaluate the performance of the algorithm, a confusion matrix was used. A binary approach (True/False) was used to ascertain whether or not the flagged scenes matched their actual quality, as shown in Table 3.

Table 3: Confusion matrix to assess fog removal algorithm's performance

Predicted		
True Negative (TN)	False Positive (FP)	Actual observation
False Negative (FN)	True positive (TP)	

Where TP (True positives) represents foggy scenes that were flagged by the algorithm, TN (True negative) represents clear (non-foggy) scenes that were flagged by the algorithm. FN (False negative) represents clear scenes that were not flagged by the algorithm. Finally, FP (False Positive) refers to foggy scenes that were not flagged by the algorithm.

The performance of the algorithm was further evaluated as shown in equation 3:

$$\text{Accuracy} = \frac{TP+TN}{TP+TN+FP+FN} \quad \text{Equation 2}$$

2.2.4. Normalization of temporal time series

Normalization is a technique used to remove the dominant daily and seasonal component on raw TIR time-series plots (Pavlidou et al., 2016). Different normalization techniques have previously been tested on TIR data. However, the two methods, namely the Background removal procedure (Sansivero et al., 2013) and STL decomposition (Cleveland et al., 1990), have been found effective in the analysis of similar datasets. The STL decomposition method requires a longer (greater than 2 years) and continuous dataset compared to the background removal technique. Owing to the limitation of the study's datasets (i.e., less than 2 years and lack of continuous datasets), the latter technique has been adopted. The technique is done chronologically as follows:

Step 1: Identification of regions of interest with contrasting thermal behavior: one consisting of the most radiant pixels (presumably affected by fumarolic activity) and another region composed of cool pixels (postulated to be affected by minimal fumarolic activities).

Step 2: Generation of time series plots of maximum apparent radiant temperature from the ROIs identified in step 1).

Step 3: Establishing the linear relationship between the maximum temperature of the thermally anomalous region (T_{max_sc}) and the corresponding maximum values of the background ROI (T_{maxBKG}) established using scatter plots.

Step 4: Fitting a trendline between values in the scatter plot; then subtract the trendline values from the Maximum value of thermally anomalous (T_{max}) ROI as shown by the following equation:

$$dt_x = T_{max(sc)} - T_{fit(x)} \quad \text{Equation 3}$$

where $dT(x)$ is the normalized temperature value, $T_{max(sc)}$ is the maximum temperature value derived from ROI of the n th TIR scene, and $T_{fit(x)}$ is the value obtained from the trend line equation of value of $T_{maxSc(n)}$ and corresponding T_{maxBKG} .

The above-mentioned procedure is illustrated in Figure 2.6.

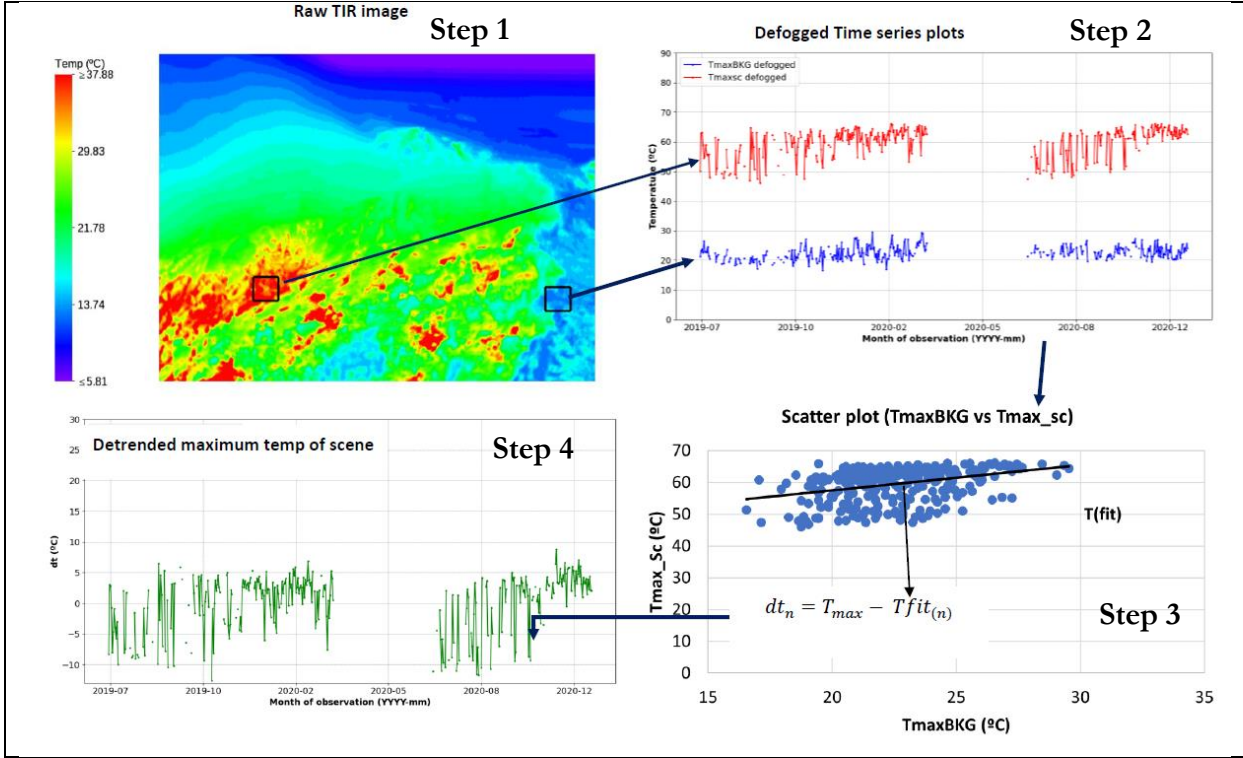


Figure 2.6: Background removal normalization procedure

The normalized temperature residuals (calculated in equation 3) are used in the estimation of heat flux (2.3)

2.3. Geothermal heat flux estimation

Heat flux is defined as subsurface heat that is transferred by fluids into the surface by conduction and convection processes (Vaughan et al., 2012). The heat flux that is recorded on the surface is a mix of the geothermal component and environmental origin, derived from reflected and re-radiated solar radiation (Mia et al., 2012).

For this study, the radiative geothermal heat-flux was calculated based on the Stefan-Boltzmann equation (Mia et al., 2012), as shown in equation 4. By using the normalized temperature values, it is assumed that the environmental affecting heat flux measurements have been removed.

$$Q_t = \epsilon MA(T)^4 \quad \text{Equation 4}$$

where Q_t is the emitted radiation in units of Wm^{-2} , σ is the Stefan-Boltzmann constant (5.667×10^{-8}), A is the area size (m^2) obtained by multiplying the pixel size by the number of pixels in a certain ROI. The pixel size estimation procedure is elaborated in section 2.3.1.

M is the emissivity of the surface materials. For this study, the emissivity of surface rhyolitic lava was assumed to be 0.9 based on measurements by Treiman et al. (2021). T is the radiant temperature (in Kelvin), calculated using the background removal procedure in equation 3.

The average radiative heat flux values (W/m^2) pixels were then plotted, analyzed, and interpreted.

2.3.1. Pixel size estimation

The size of a single-pixel in image space, also referred to as Ground Sampling Distance (GSD), can be calculated for nadir and oblique views. In this study, the GSD was estimated based on the approach by Balamuralidhar et al. (2021) shown in Equation 5. The initial step assumes nadir orientation and specific camera parameters (see Table 1).

$$GSD = \frac{SW \times WD}{FL \times IW} \quad \text{Equation 5}$$

Where GSD is the ground sampling distance or pixel size, SW is the width of the thermal infrared camera's sensor (mm); find value in

Table 1, WD is the approximate distance between camera and target (find value in

Table 1); estimated from a Google Earth platform (see Figure 2.7), FL is the focal length of thermal infrared camera (mm); find value in

Table 1., IW (image width) is the number of pixels in the thermal infrared camera's image resolution (find value in

Table 1).

Owing to the oblique camera orientation (see Figure 2.1-A), the second step was to convert the nadir pixel size (calculated in equation 5) into off-nadir context by multiplying it with GSD Rate as shown in Equation 6.

$$GSD_{\text{Rate}} = \frac{1}{\cos(\theta + \phi)} \quad \text{Equation 6}$$

Where θ is the camera tilt, ϕ describes the angle of field of view. In this study, θ is estimated at 45° , while ϕ is 34° based on field of view specifications shown in Table 1.

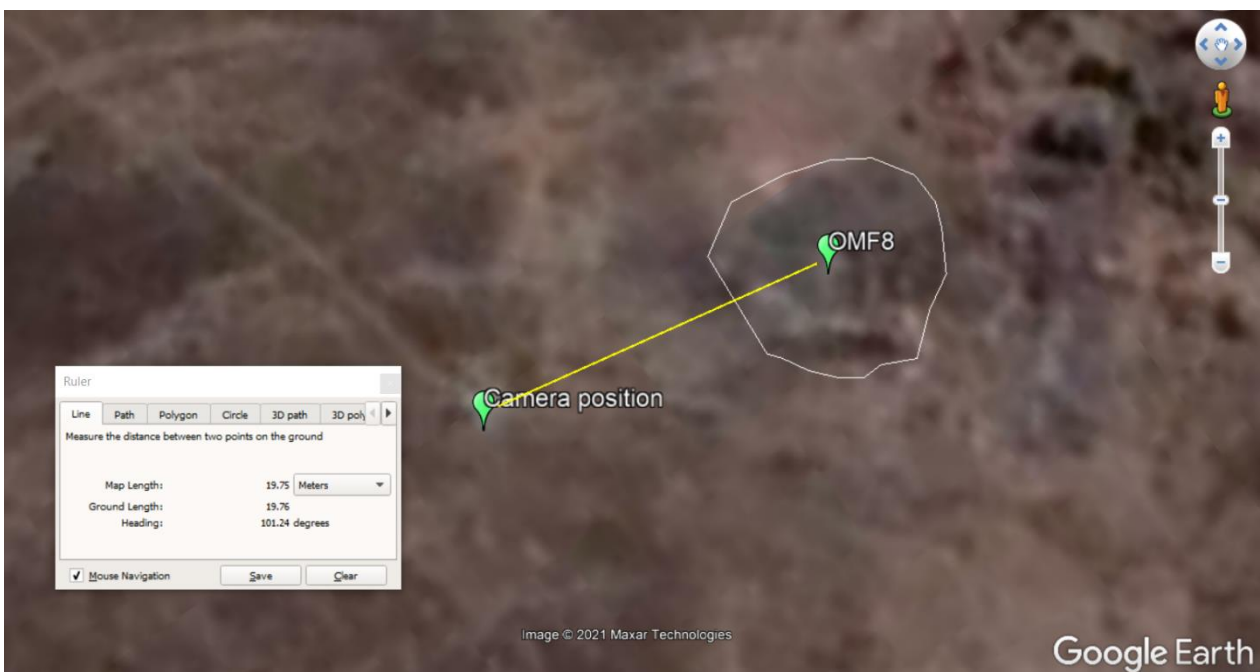


Figure 2.7: Estimated distance between the thermal camera and OMF8 on the Google Earth Pro platform. The camera is oriented in a relative N-S position.

2.4. Analysis of gas discharge chemistry data

In this step, the temporal variation of fumarole gas discharge chemical constituents was analyzed to proxy geothermal reservoir processes such as boiling, mixing, and hydrothermal degassing. Therefore, the analysis was done as follows:

1. Creation and analysis of temporal time series plots of major gaseous components (CO_2 and H_2S) over the entire period.
2. Creation of time series plots of chloride concentration of different periods of observation. The plots were then analyzed for any unusual behavior (of peaks and troughs).
3. Grouping of the above gas components based on the period of observation. Due to the low temporal resolution of the datasets, the grouping was done per year of observation. After that, the statistical distribution of yearly values was analyzed using clustered box plots. A trend line was fitted along with the mean values, and the overall trend was assessed.

3. RESULTS

3.1. Spatial subsets into regions of interest

The aim of this section is to demarcate the specific hour-of-day time TIR scenes into regions of interest that are affected by geothermal and non-geothermal influences. These results address the first objective of the study. The findings are presented as follows: principal component analysis (3.1.1), analysis of temporal mean and standard deviation (3.1.2), and analysis of time series plots of specific ROIs (3.1.3).

3.1.1. Principal component analysis (PCA)

Principal Component Analysis products of different hour-of-day TIR images are shown in Figure 3.1 (a-e). In this study, three principal components were taken for this data set, which possesses over 99% of the total proportion of data variance (**Appendix 1**). The time-lapse camera optical image (Figure 3.1 f) has been used as a ground truth tool to provide the context of zones with contrasting colored pixels of PCA images. PCA images show different regions with spatial contrast based on the distribution of homogeneously colored pixels (labeled using equally shaped polygons).

For example, the reddish-brown to purple colored pixels of the PCA images (labeled 1) corresponds to rock debris at the foot of the fumarole (south western regions of time-lapse camera image). In addition, the purplish to light green pixels (labeled 2) correspond to vegetated sections in the area's southern portion. The greenish-colored pixels (labeled 3) mainly correspond to unconsolidated soils, constituting most of the land cover of the focus area. Finally, purplish to dark green colored pixels (labeled 4) of PCA image relates to the eastern portion of the focus area.

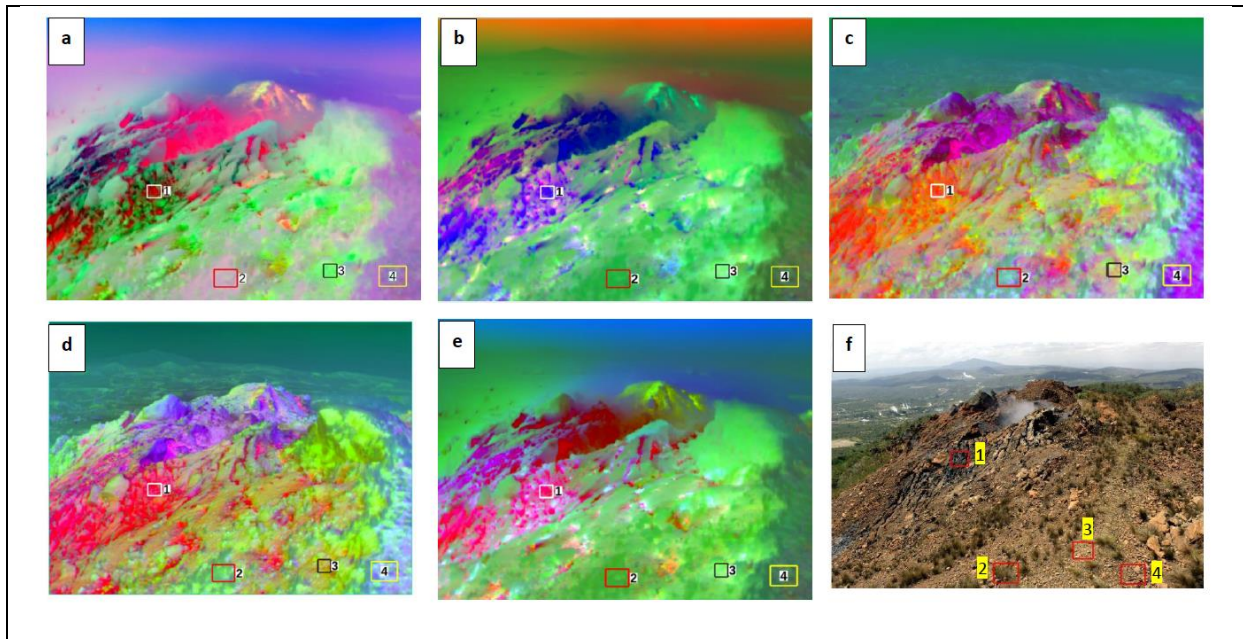


Figure 3.1: Band combination RGB=Principal Components 123 of TIR images acquired at (a) 00:00 UTC, (b) 03:00 UTC, (c) 09:00 UTC, (d) 12:00 UTC and (e) 21:00 UTC. (f) is an optical time-lapse camera image of the area acquired at 09:00 UTC. Polygons 1-4 represent zones with homogeneously colored pixels, selected based on visual inspection of the time-lapse optical image and considering other factors such as relative slope orientation and surface material variability.

Polygons are overlaid over other products (temporal mean and standard deviation images) to demarcate regions of interest for subsequent analysis, as discussed in the next section.

3.1.2. Temporal mean and standard deviation

Figure 3.2 (a-e) shows the temporal mean radiant temperature of the selected hour of day TIR images and corresponding time-lapse camera image of the area of focus. It observed that the spatial distribution of radiant surface temperature on the ROIs varies across different hours of acquisition. The central, southwestern parts of the images (labeled 1) exhibit the highest radiant temperature values across all hours of acquisition. Some high-temperature pockets are also seen (highlighted by black circles) in the south-eastern part of the image. They tend to be pronounced during the day, especially at 09:00 UTC. Low radiant temperature values (blue colored) are observed in the northern and eastern (labeled 4) and southern (labeled 2) parts of the image. These values in the western and southern regions increases during the day, particularly at 09:00 UTC. Medium temporal mean radiant temperature values (25.3-35.0) are observed over the northern portions of the images (near the fumarole vent area), remain constant over different hours of acquisition. The estimated spatial mean temperature values bounded by the polygons (labeled 1-4) of different hour-of-day temporal images of acquisition are shown in Table 4. For the sake of consistency, the polygons are named ROI-1, ROI-2, ROI-3, and ROI-4, respectively.

Generally, ROI-1 has the highest surface radiant temperature values, followed by ROI-3, ROI-2, and ROI-4.

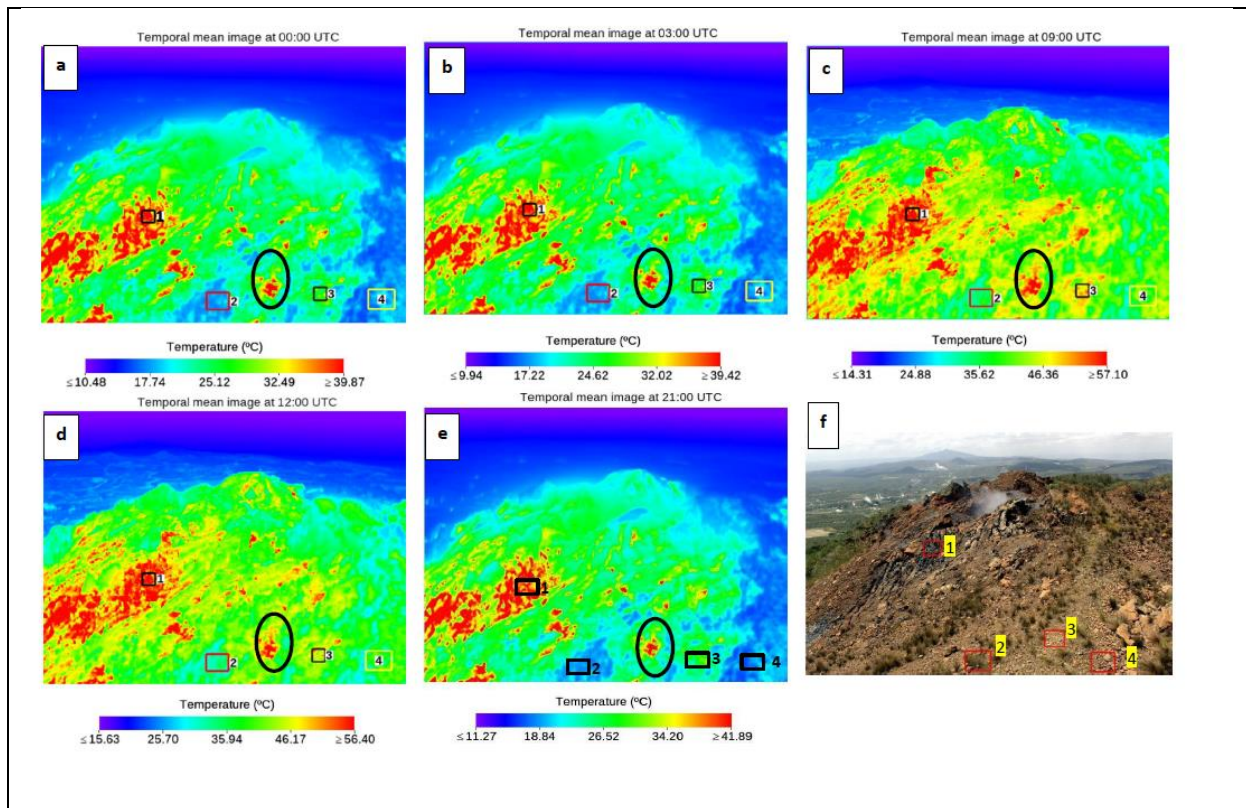


Figure 3.2: Temporal mean of TIR images acquired at (a)00:00 UTC, (b)03:00 UTC, (c)09:00 UTC, (d)12:00 UTC and (e)21:00 UTC. Polygons 1-4 represent different ROIs generated by demarcating homogeneously colored pixels of PCA images.(f) is an a time lapse optical image acquired at 09:00 UTC. Pockets of high radiant temperature pixels across different hour-of-day images are highlighted using black oval shapes.

Table 4: Measured surface radiant temperature distribution across different ROIs of selected hour-of-day temporal mean images

ROI	Temperature per hour of the day (°C)					Temp values of ROIs at different hour-of-day
	00:00	03:00	09:00	12:00	21:00	
ROI-1	39.9	39.4	57.1	56.4	41.9	46.9
ROI-2	17.7	17.2	35.6	35.9	18.8	25.0
ROI-3	25.1	32.0	46.4	46.2	34.2	36.8
ROI-4	17.7	17.2	35.6	35.9	11.3	23.6

The polygons (ROIs) are overlaid over various standard deviation images as described in the next paragraphs. Figure 3.3 (a-e) shows the spatial distribution of standard deviation of the radiant temperature of different hour-of-day TIR images. The time-lapse camera image (Figure 3.3 f) has been used to contextualize the various standard deviation values with real surface objects of the focus area. The results show varying spatial contrast of standard deviation values of different surface materials over different hours of acquisition. For instance, the southwestern parts of the images (ROI-1), corresponding to the hottest part of the fumarole, exhibit the high standard deviation values across all hours of acquisition, except at 12:00 UTC; where western zones exhibit high standard deviation values.

The lowest standard deviation values are of night-time TIR scenes (00:00, 03:00, and 21:00 UTC) are seen over the western (ROI-4) and southern (labeled ROI-2) parts of the image. However, these values increase during the day and are highest at 12:00 UTC. In addition, the northern parts (mainly sky and other background areas) have low values at 12:00 UTC, compared to other hours of acquisition. The estimated standard deviation values of selected ROIs of different hour-of-day time series TIR images are shown in Table 5. The highest values are seen over ROI-1, followed by ROI-3, ROI-4, and ROI-2, respectively.

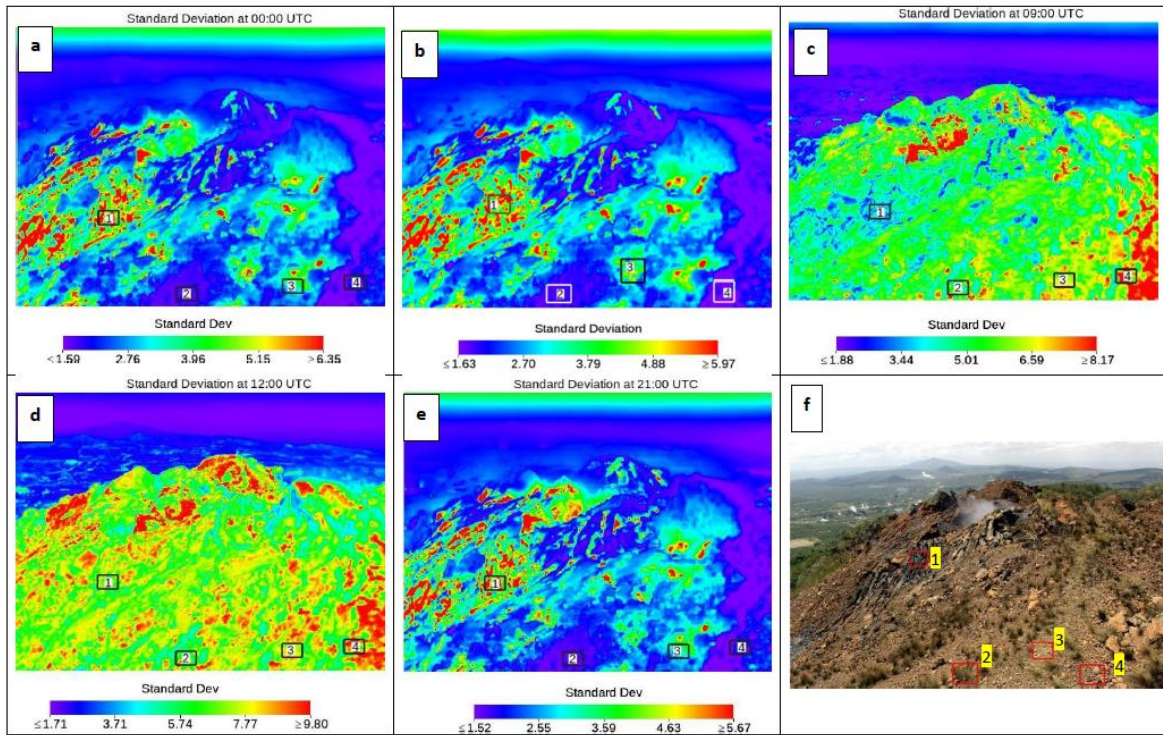


Figure 3.3: Temporal standard deviation of TIR images acquired at (a) 00:00 UTC, (b) 03:00 UTC, (c) 09:00 UTC, (d) 12:00 UTC and (e) 21:00 UTC. Polygons 1-4 represent different ROIs generated by demarcating homogeneously coloured pixels of PCA images. (f) is a time lapse optical image acquired at 09:00 UTC.

Table 5 Standard deviation distribution across different ROIs of selected hour-of-day

ROI	Standard deviation per hour of the day					Average standard deviation values of ROIs at different hour-of-day
	00:00	03:00	09:00	12:00	21:00	
ROI-1	6.35	4.88	3.44	7.77	5.74	5.6
ROI-2	1.59	2.70	5.01	5.74	1.52	3.3
ROI-3	3.96	3.79	6.59	7.77	3.59	5.1
ROI-4	1.59	1.63	8.17	7.77	1.52	4.1

Time series of minimum, maximum, mean are extracted from the different ROIs to further assess the temporal, discussed in the next section.

3.1.3. Radiant temperature time series across different ROIs

This section describes the time series plots of specific ROIs of different hour-of-day TIR images and their relationship with ambient weather conditions (air temperature and precipitation). In this section, the time series plots of the 00:00 UTC and 09:00 UTC are being presented; as a representative of daytime and night surface radiant temperature temporal behavior. Time series plots of other hour-of-day scenes are shown in Appendices (1-3).

Temperature variation in ROI-4

Figure 3.4 (A-B) shows the daily average minimum/maximum/mean radiant temperature, air temperature, and precipitation (mm) of ROI-4 acquired at 00:00 UTC between July 2019 to December 2020. The time series plots show a variation with seasonality. In addition, the minimum, maximum, mean, and standard deviation values of the 00:00 UTC time series plots are lower than those of 09:00 UTC. The minimum radiant time series plot of the 00:00 UTC is consistent with the air temperature, with a coefficient of determination (R^2) of 0.1891 (Appendix 5-i).

On the other hand, the time series plot of the 09:00 UTC hour-of-day scenes is higher than the air temperature plots. They also have a lower coefficient of determination (R^2) of 0.1015 (Appendix 5-ii).

A drop in temperature peak values of time series plots is observed during rainy periods for both 00:00 and 09:00 UTC. This is evident between September, December 2019, and October 2020 (highlighted using black arrows).

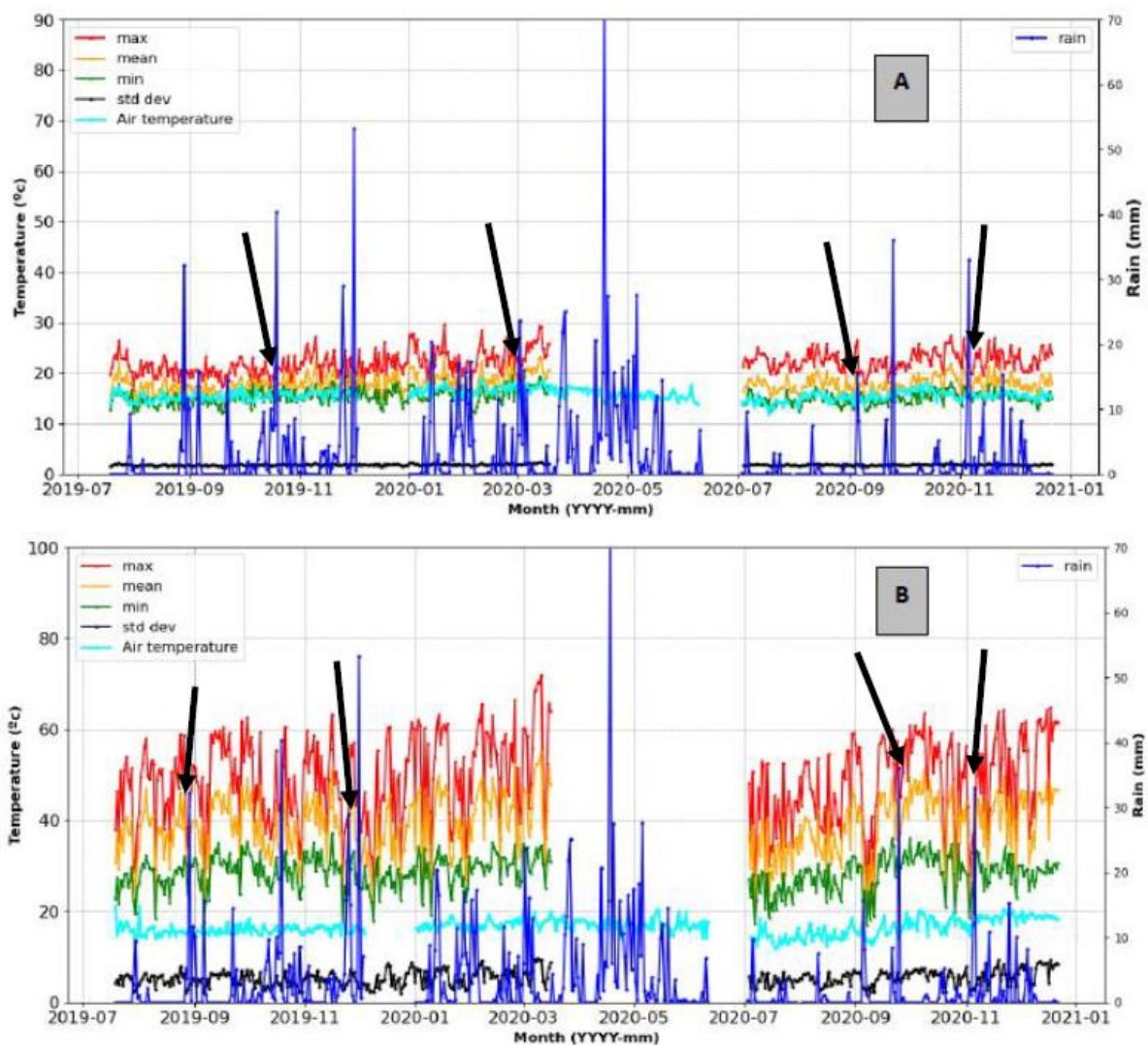


Figure 3.4: Variation of minimum, maximum, mean, and standard deviation apparent temperature values of ROI-4 at (A) 00:00 UTC and (B) 09:00 UTC, in combination with hourly air temperature and daily rainfall and air temperature for the period 2019-2020. The arrows show periods with a decline in apparent radiant temperature values due to precipitation.

Temperature variation in ROI-3

The time plot of radiant temperature and corresponding weather values of ROI-3 is shown in Figure 3.5 (A-B). Similar to ROI-4, the radiant temperature time series plots variation (peaks and troughs) with seasonality (i.e., irregular peaks and troughs over time). However, the ranges of radiant temperature values of 00:00 UTC are lower than 09:00 UTC, varying between 8-12 °C (minimum), 8-13 °C (mean), and 21-27 °C (maximum). The 09:00 UTC values mainly ranges between 17-40 °C (minimum), 23-65 °C (maximum), 18.0-46 °C (mean).

Like the ROI-4, the relative distance between the minimum, maximum, and mean values of 00:00 UTC plots are lower than the 09:00 UTC, with a coefficient of determinations (R^2) of 0.1002 and 0.0242, respectively (**Appendix 5-iii** and iv). Finally, similar effects of rainfall on time series plot values are also evident in this ROI's plots, as highlighted by black arrows.

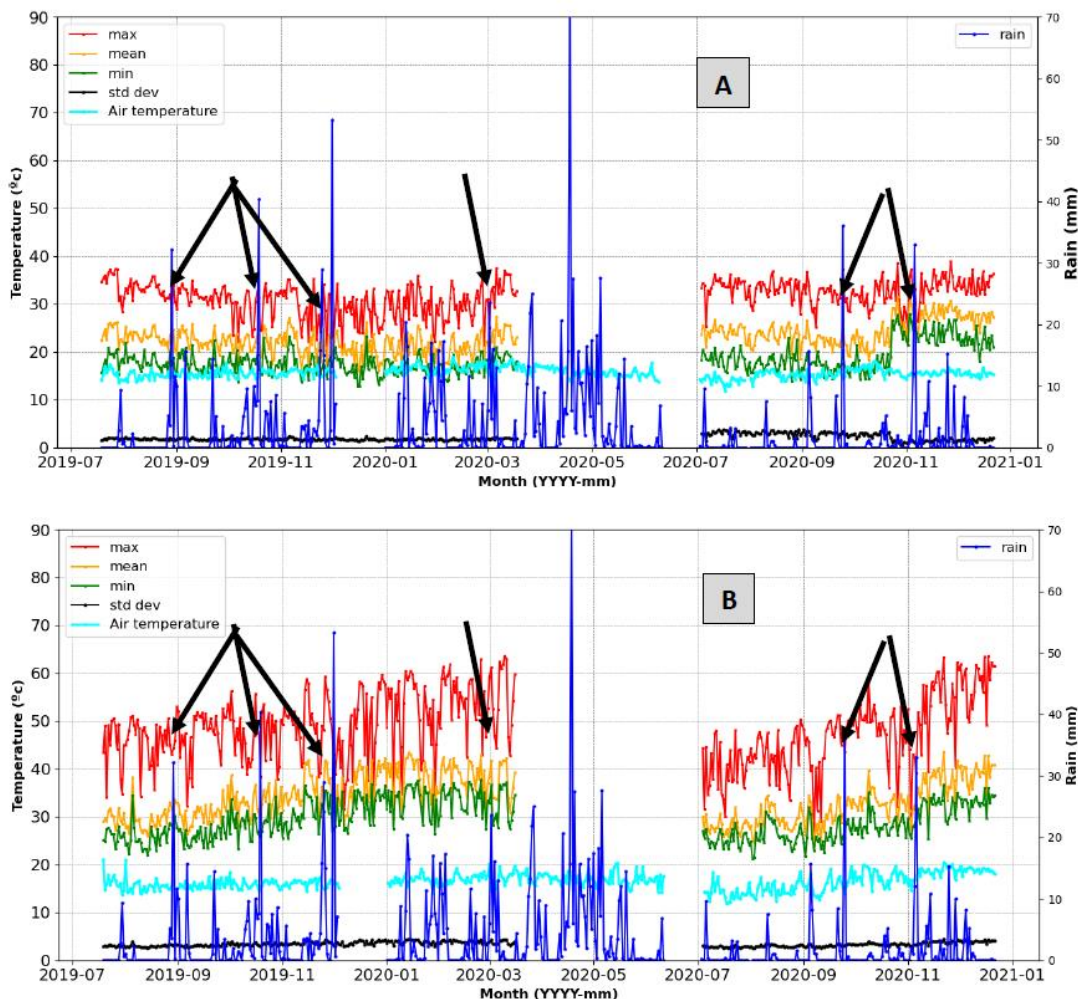


Figure 3.5 : Variation of minimum, maximum, mean, and standard deviation apparent temperature values of ROI-3 at (A) 00:00 UTC and (B) 09:00 UTC, combined with hourly air temperature and daily rainfall and air temperature for the period 2019-2020. The arrows show periods with a decline in apparent radiant temperature values due to precipitation.

Temperature variation in ROI-2

The time series plots of radiant temperature and corresponding weather values of ROI-2 (Figure 3.6) show similar temporal behavior with other background ROIs (i.e., ROI-4 and ROI-3).

However, their radiant temperature values are higher compared to ROI-4 and ROI-3. The air temperature values are lower than the minimum radiant temperatures for both 00:00 UTC and 09:00 UTC plots. There is no correlation between the air temperature and minimum radiant temperature values (see **Appendix 5(v-vi)**).

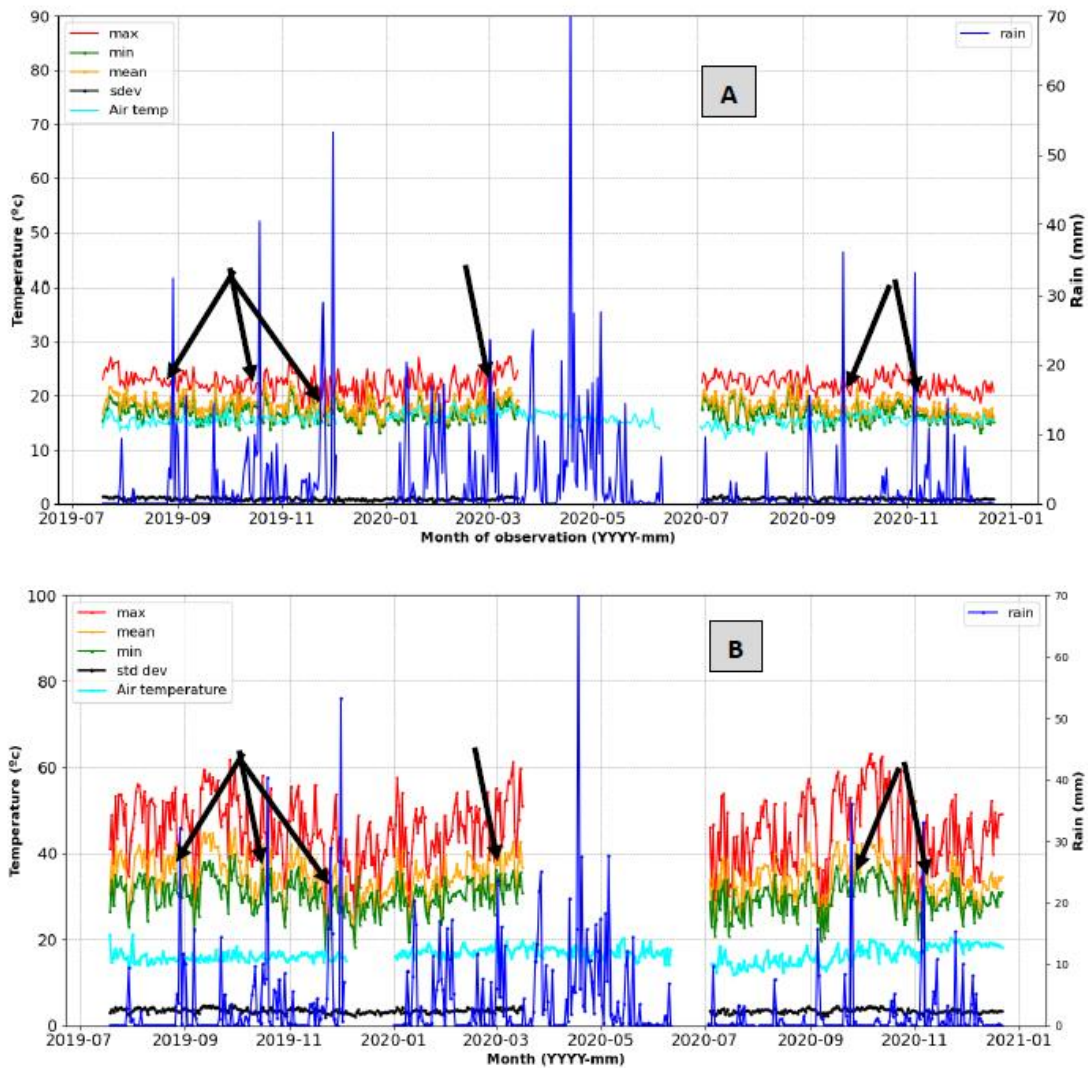


Figure 3.6: Variation of minimum, maximum, mean, and standard deviation apparent temperature values of ROI-2 at (A) 00:00 UTC and (B) 09:00 UTC, combined with hourly air temperature and daily rainfall and air temperature for the period 2019-2020. The arrows show periods with a decline in apparent radiant temperature values due to precipitation.

Temperature variation in ROI-1

Finally, the time series plots of values in ROI-1 (Figure 3.7) are described. They also show irregular variations of peaks and troughs with time. Their radiant temperature values are highest compared to other ROIs. One notable observation in this ROI is that they show the highest enhanced seasonal variation (highlighted by black arrows).

For instance, the average radiant temperature value of pixels recorded between consecutive days differs by over 40 °C.

Lastly, the minimum radiant temperature values are higher than the air temperature, with a coefficient of determination (R^2) of 0.0326 and 0.0045 for 00:00 and 09:00 UTC, respectively (**Appendix 5 vii-viii**).

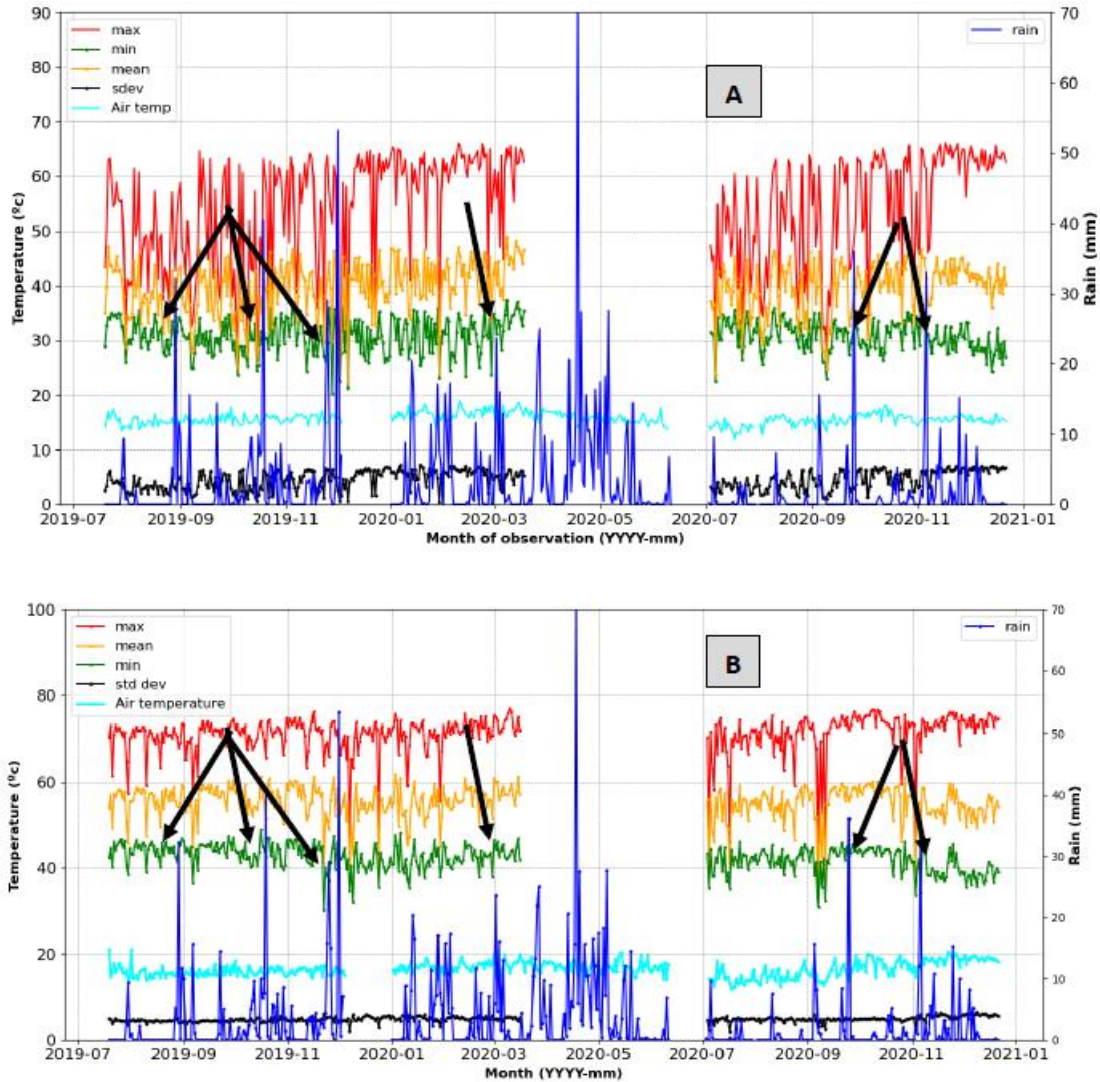


Figure 3.7: Variation of minimum, maximum, mean, and standard deviation apparent temperature values of ROI-1 at (A) 00:00 UTC and (B) 09:00 UTC, in combination with hourly air temperature and daily rainfall and air temperature for the period 2019-2020. The arrows show periods with a decline in apparent radiant temperature values due to precipitation.

In summary, the following are the key take-aways from section 3.1.3:

- ROI-1 has the highest instability of values in temporal space, signified by the highest periodic variation of the time series plot values. Its radiant temperature values have the least influence on air temperature, signified by the lowest coefficients of determination.

- ROI-4 has the highest stability of values in temporal space, as shown by the highest consistency between minimum, maximum, and meantime series plots. In addition, these values have the strongest influence on air temperature, signified by the highest coefficients of determination.

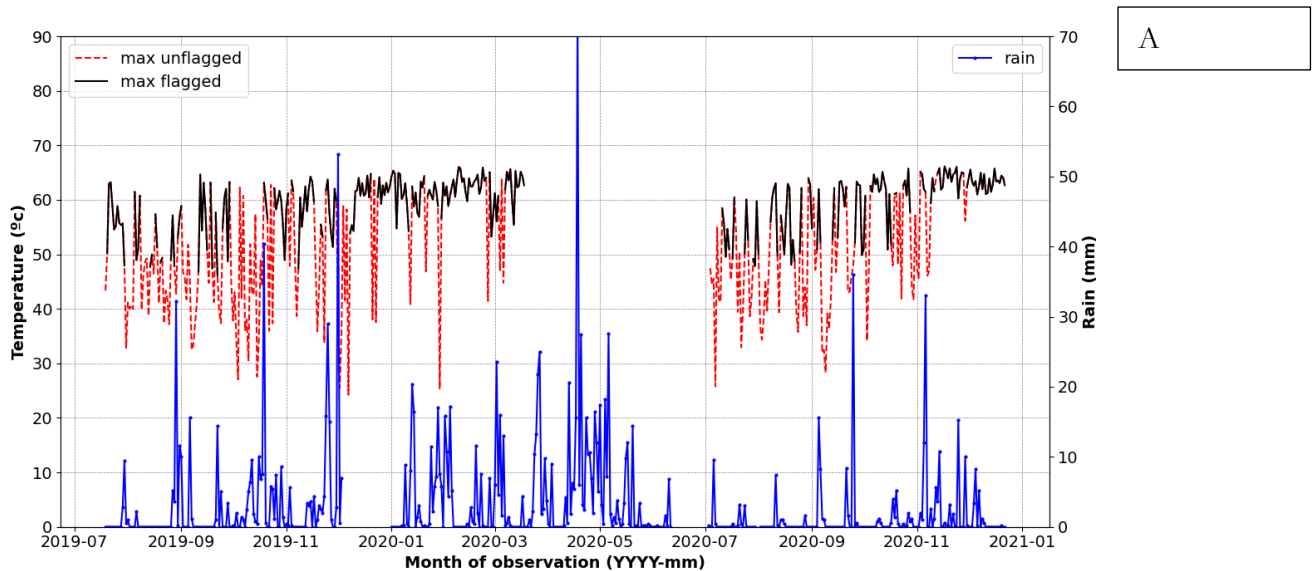
As such, the temporal values of the two ROIs (represents extreme conditions) have been used for subsequent analysis.

3.2. Foggy scenes removal

This section presents the results of flagging anomalous radiant temperature signals associated with foggy TIR scenes. This was done using a foggy images detection algorithm based on standard deviations of all pixels of selected hour-of-day TIR scenes. The algorithm’s findings are summarized in Table 6. It is shown that more night-time values are flagged compared to daytime scenes. In addition, the flagged values correspond to low radiant temperature signal values, mainly dominant in pixel values of ROI-1, as demonstrated by time plots in Figure 3.8 A. The precipitation-induced rapidly varying peaks and troughs (dotted lines) of the raw time series value plots have been flagged. The effects are more pronounced on the night-time plots(Figure 3.8 A) than day-time plots (Figure 3.8 B). However, the overall trends of the time series plots devoid of foggy scenes do not change. The time series plots (minus foggy scenes) for other hour-of-day acquisitions are shown in **Appendix 6**.

Table 6: Summary of TIR scenes flagged by algorithm

Time	00:00 UTC	03:00 UTC	09:00 UTC	12:00 UTC	21:00 UTC
No of flagged scenes	115	98	42	22	108
Sample size	416	416	416	416	416



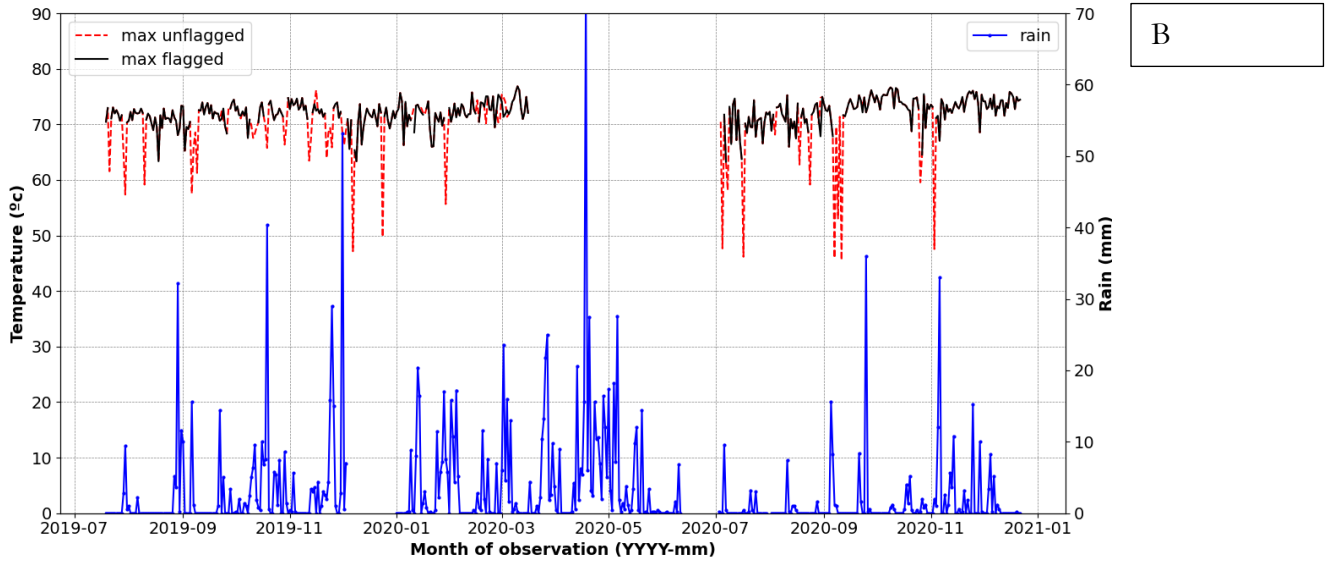


Figure 3.8: Time series plots of original (red dotted colors) TIR images (with foggy scenes) and without foggy scenes (black line) graphs of ROI-1 at (A) 00:00 UTC and (B) 09:00 UTC.

3.2.1. Evaluation of fog removal algorithm's performance

The performance of the algorithm is represented using a confusion matrix in Table 7 and Table 8. From Table 7 (00:00 UTC), out of 115 flagged scenes, 100 were correctly flagged (True Positives), and 3 were classified as clear (False Negatives). On the contrary, out of 313 unflagged scenes, 300 were clear (True negatives), while 13 were foggy (False positives).

On the other hand, the confusion matrix of Table 8 (09:00 UTC) shows that out of 42 flagged scenes, 15 had fog (True Positives), while 27 were clear (False Negative). In contrast, out of 374 unflagged scenes, 303 were clear (True negatives), while 71 were foggy (False positives).

Table 7: Confusion matrix showing performance of the algorithm on 00:00 UTC TIR scenes

Predicted		Actual observation
250 (TN)	15 (FP)	
15 (FN)	100 (TP)	
Accuracy $(\text{TP} + \text{TN} / \text{TP} + \text{TN} + \text{FP} + \text{FN})$		84%

Table 8: Table 3.4: Confusion matrix showing performance of algorithm on 09:00 UTC TIR scenes

Predicted

303 (TN)	71 (FP)
27 (FN)	15 (TP)
Accuracy ($\frac{TP + TN}{TP + TN + FP + FN}$)	76%

Actual
observation

3.3. Time series normalization

The results of time series normalization (based on background procedure) of maximum apparent radiant temperature values of ROI-1 and ROI-4 are shown in Figure 3.9. Both normalized time series plots show seasonality variation, with irregular random fluctuations (highlighted using black circle) between July 2019 and March 2020. It is then followed by a gradual increase between July to November 2020.

Finally, sharp peaks (labeled using black arrows) are observed on the 09:00 UTC time series plots between July 2019, March 2020, and December 2020.

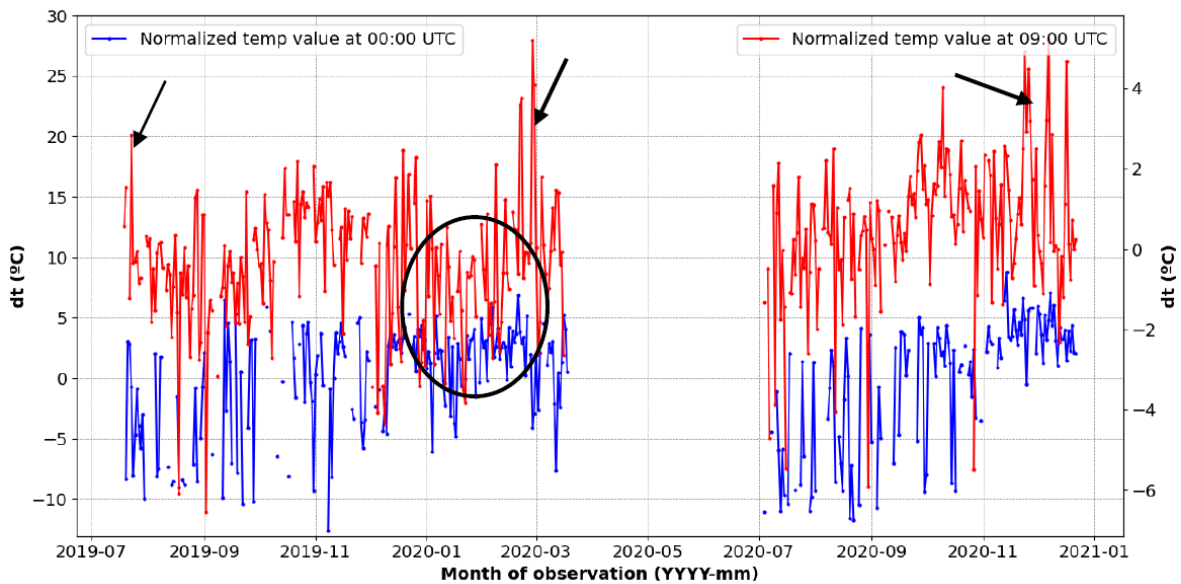


Figure 3.9: Time series plots of normalized (background removal procedure) maximum apparent radiant temperatures values at 00:00 UTC (blue) and 09:00 UTC (red). The black circles shows the time window characterized by fluctuation of time series values. The black arrows show periods characterized by anomalous peaks values.

3.4. Geothermal heat flux estimation

The time series plots results of geothermal heat flux estimations are shown in Figure 3.10. The heat flux plots have been generated using normalized maximum radiant temperature (section 3.3), thus representing the focus area's

subsurface emission's temporal behavior. The time series plots (00:00 UTC and 09:00 UTC) show a similar pattern of variability with the normalized time-series plots (Figure 3.9).

The heat flux values of 00:00 UTC plots (blue colored) are higher than 09:00 UTC. They also show a higher variation of peaks and troughs compared to the 09:00 UTC plots.

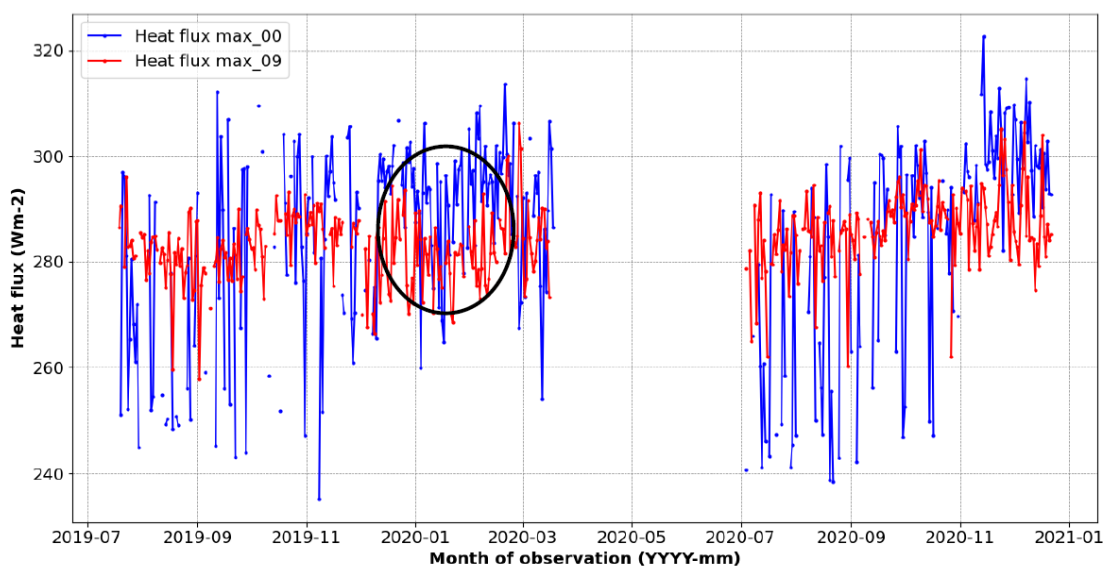


Figure 3.10: Heat flux plots of detrended surface radiant temperature of TIR scenes at 00:00 UTC (blue color) and 09:00 UTC (red color). The period highlighted by black circle is characterized by occasional random variability.

3.5. Analysis of gas discharge chemistry data

This section presents the findings of the temporal variation of fumarole gas chemical concentration.

To start with, the overview of gas concentration measurements is outlined in **Appendix 7**. The data consist of the gaseous component (CO_2 , H_2S , SiO_2) and non-gaseous parameters constituting, e.g., Ca, Li, Na, Cl, SO_4 , and K. Data gaps are observed in the SO_4 , Cl, Na, and Li columns. The analysis of the temporal variation of selected fumarole gas parameters is discussed in sections 3.5.1 and 3.5.2.

3.5.1. Temporal variation of CO_2 , H_2S , and chloride

The time series plots of two gases (CO_2 and H_2S) between 2008 to 2020 are shown in Figure 3.11 (A). Their time series plots vary considerably during the period of observation. Some peak signals of both gases were observed between 2009, mid-2010, late 2013, 2014, and mid-2020. The plot values were relatively stable between mid-2015 to 2018.

On the other hand, the chloride plot (Figure 3.11 B) values vary considerably during the observation time, with occasional peaks in 2012, 2016, and 2020.

The grouped plots (**Appendix 8**) also show a similar temporal pattern with raw value plots described in the previous paragraphs.

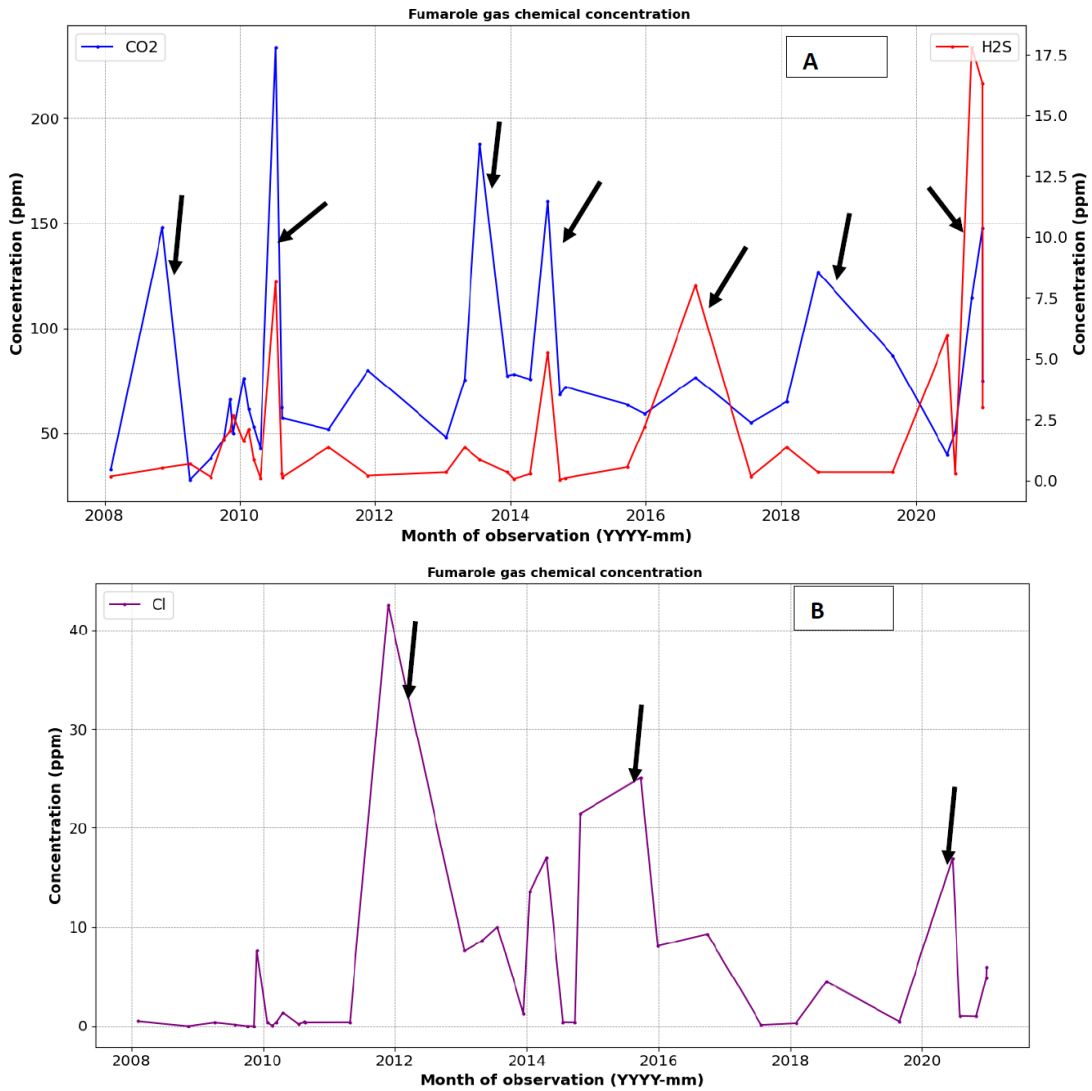


Figure 3.11: (A) Temporal variation of CO₂ and H₂S between and (B) chloride for the period 2008 to 2020. The black arrows time periods with peaks of the fumarole gas components.

4. DISCUSSION

4.1. Discussion of spatial subset into ROIs

The spatial distribution of pixels of various indicator products, e.g., principal component analysis, temporal mean, and standard deviation, can be used for preliminary identification of areas affected by environmental (e.g., fog, rain, solar illumination) and fumarole activity (geothermal) effects. The findings are discussed in the subsequent paragraphs.

To begin with, the subtle spatial patterns discernible on PCA composite images through homogeneously are useful in exploratory analysis (see Figure 3.1 a-e). These similar colored spatial patterns (denoted using polygons) depict the overall behavior of few uncorrelated principal component products, with the highest variance (see **Appendix 1**). Although such patterns spatially compare with those of time-lapse cameras, inference cannot be made solely based on visual inspection of the spatial distribution of the colored pixels.

The use of other products, i.e., temporal mean (Figure 3.2 a-e) and standard deviation (Figure 3.3 a-e), give a better overview of the thermal behavior of surface material in the area of focus. Observing the general spatial distribution and stability of pixel values across different acquisition hours made it possible to determine which part of the area was affected by environmental and fumarole activity. For example, the results show the highest temporal mean and standard deviation values in sections near the main fumarole area and surrounding rock debris (ROI-1) across different hours of acquisition. Such behavior can be attributed to pronounced effects of fumarole activity on these regions, which are of geothermal origin based on the study's hypothesis. In contrast, the other regions whose temporal mean and standard deviation values are lower relative to those near the main fumarole area have reduced effects of fumarole activity. It is also assumed that environmental effects are more pronounced in these areas than in thermally anomalous regions. As such, the eastern part of the study area (ROI-4) with the lowest temporal mean and standard deviation values across different hours of acquisitions are deemed to have the strongest influences of environmental effects, hence most suitable for control purposes. However, one limitation with the standard deviation products is that it shows some inconsistencies in values distribution across specific day hours. For instance, reversal of values experienced at 12:00 UTC hour-of-day image (Figure 3.3 e) emphasizes its unreliability to demarcate external influences when the ground has attained optimal heating.

The temporal statistics (minimum, maximum, mean, standard deviation) of selected ROIs of specific hour-of-day TIR images (Figure 3.4 to Figure 3.9) were useful to assess the temporal behavior and stability of the surface temperatures over time. In this study, all the time series plots of different ROIs depict seasonal variability across different hours of acquisition. The seasonal variation can be attributed to the effects of environmental factors on the apparent temperature values. It is also shown that variability depends on specific ROI. For example, seasonal variability is most pronounced on apparent temperature values of ROI-1 (main fumarole area), implying that they

have the highest instability across different hours of acquisition. Such instability is an indication that the surface temperature of materials in these ROI are strongly affected by ambient weather conditions. Moreover, the rapid fluctuation of temporal plots during rainy periods indicates that precipitation is the main external factor controlling the recorded apparent radiant temperatures. In general, precipitation is known to induce cooling effects on the surface temperature, implying that the recorded apparent temperatures of this ROI are underestimated (Zimmer et al., 2017).

The dependence of TIR radiant temperature and air temperature has also been statistically tested, as shown by scatter plots in **Appendix 5**, assuming that the dynamics of air temperature and surface temperature interactions affect the emitted radiance. In this regard, a high coefficient of determination between the minimum radiant temperature in a specific ROI and hourly air temperature implies a strong dependence on ambient conditions resulting in decreased surface emittance. As such, the highest correlation between minimum radiant temperature and air temperature is observed in pixels of ROI-4 (**Appendix 5-i**), implying that they experience the strongest control of ambient weather conditions relative to other regions. On the contrary, the absence of correlation between ambient air temperature and minimum radiant temperature of pixels in the thermally anomalous zones (**Appendix 5-vii**) suggests that factors other than air temperature affect their variability.

The temporal and spatial behavior of other ROIs (i.e., vegetation (ROI-3), unconsolidated pyroclastic debris (ROI-2)) is unstable over different hours of the day. Such instability can be attributed to effects of surface materials mainly results from varying thermal inertia properties of different land surface materials within specific ROIs. For example, the vegetated pixels have lower seasonal variability across different hours of observation. However, these variations can be attributed to other processes such as evapotranspiration that compromise such values' reliability for analysis purposes. Finally, the relative instability of unconsolidated pyroclastic materials can be attributed to differential heating due to thermal inertia, which is also higher than the vegetation pixels. Owing to the above-mentioned factors, the time series plots of thermally anomalous ROI and those at the eastern part of the area of focus were therefore considered suitable for subsequent analysis.

4.2. Discussion of fog removal thresholding algorithm

The thresholding algorithm (equation 1) was used to isolate signals associated with specific hour-of-day TIR images acquired during foggy conditions. The number of flagged signals at night was higher than during the day (Table 6). This can be attributed to higher homogenization effects (signified by low standard deviation) experienced at night than during the day (Chiodini et al., 2007). This effect increases the absorption of thermal infrared signals, leading to underestimating apparent temperature values recorded by the thermal camera (Stevenson et al., 2008). Consequently, more outlier signals are notes at night compared to daytime.

The accuracy of the thresholding algorithm also depended on the time of acquisition; higher accuracy is attained on night-time scenes than daytime acquisitions (see Table 7 and Table 8). The following reasons can be for the errors above is discussed as follows:

- The thresholding algorithm adopts a distribution-based outlier detection approach (Kou et al., 2006). This implies that observations (i.e., standard deviation) with unusual behavior within the frequency distribution are always considered outliers. For example, clear TIR images acquired during cloudy days, characterized by lower standard deviation values, are considered anomalous, compared to others acquired during sunny conditions, therefore flagged. In other instances, for example during colder months (between July-September 2020), a slight increase in temperature values of specific periods is considered anomalous compared to other observations, therefore flagged.

4.3. Discussion of time series normalization

The normalization process further suppressed extreme values from time series plots, resulting in smoothed time-series plots (see Figure 3.9 and **Appendix 6**). However, cyclic effects are signified by irregular fluctuations observed on the normalized time series plots. Such fluctuations are attributed to exogenous effects that arise from short precipitation episodes between November to December 2020. Such conditions impose homogenization conditions (discussed in section 4.2), implying an increased number of foggy TIR scenes and corresponding false outlier signals. Such periods are generally typified by an increased number of foggy scenes' radiant temperature values that were not flagged by the fog-removal algorithm.

Another reason for the irregular fluctuation could be the choice of ROI identified in the normalization procedure. In general, the success of this normalization procedure depends on the homogeneity of the land surface materials of specific ROIs (Sansivero et al., 2013). The method assumes spatial autocorrelation (i.e., the high similarity of radiant temperature values in a specific ROI). For instance, if the thermally anomalous ROI (e.g., ROI-1) has some less emissive materials (e.g., pyroclastic rubble), the overall average apparent value tends to be underestimated, which affects the selected (T_{max}) value used in the normalization process. The same applies to other ROIs.

4.4. Discussion of heat flux estimation and implications on the geothermal motor

It is noted that there is a similarity in trend between the heat flux plots (Figure 3.10) and normalized temperature plots (Figure 3.9). This similarity is an indication that the heat loss is sensitive to temperature changes of the surface. Nevertheless, the temporal behavior of heat flux plots (Figure 3.10) represents the heat emitted from the surface and is postulated to characterize the subsurface behavior of the geothermal system, thus linked to the 'geothermal motor' activities. The following interpretations can be made from the heat flux time series plots:

- The irregular random variations (between October to November 2019) are a factor of weather, specifically precipitation. Precipitation generally causes surface cooling, which lowers the apparent radiant temperature values, implying that the estimated heat flux values are lower than those recorded during dry

periods (Mia et al., 2012). Within the Olkaria geothermal field, reduced heat flux has been associated with an influx of cold fluids along downflow zones, i.e., mainly along the fault axis (Ofwona, 2002). Such scenario is evidenced by reduced steam discharge along fumarole vents (e.g., East field), majorly attributed to a decrease in the boiling of reservoir fluids by the infiltrating fluids (Axelsson et al., 2013), postulated to decrease the geothermal motor speed. Another possible reason for the periodic variation of heat flux plot values is the oscillation of fluids in a shallow hydrothermal system (Spampinato et al., 2012), which prompts cyclic emission of heat into the surface. In the Olkaria geothermal field, such events are triggered by magma degassing (West jec, 2009), which is manifested by the cyclic variation of enthalpies in the wells around the neighbouring fields as OW-39A and OW-201 (Wamalwa et al., 2016).

- The period characterized by an increase in trend (July to August 2020) can be associated with increased heat discharge, which, according to Mia et al. (2012), increases agitation of subsurface fluids, evidenced by increased emitted heat through the fumarole vent opening.

Within the Olkaria field, such activities have been linked with increased steam discharge through permeable structures of deep up-flow zones, especially the N-S faults of the Olkaria East field (Axelsson et al., 2013), where the fumarole of focus is situated. Since the movement of fluids is convective, such episodes signify an increase in discharge, which, based on the study's hypothesis, increases the speed of the geothermal motor.

- The periods of near-constant trend (July to November 2019) might be linked by the quiescent phase of a magmatic system (Spampinato et al., 2012). Previous studies, e.g., Axelsson et al. (2013), have associated such events with a reduction in movements of fluids within geothermal systems. In a productive geothermal setup (e.g., Olkaria field), such period can be attributed to reduced extraction of the geothermal resource or even phases where production wells are shut for maintenance (Ouma et al., 2016). Based on the study's hypothesis, events signifies phases with reduced geothermal motor speed.

4.5. Discussion of gas geochemistry

The time series plots of selected fumarole gas chemical components (i.e., CO₂, H₂S, and chloride (Cl)) in Figure 3.11 show variability with occasional spikes between consecutive observations. Although the spikes are postulated to be contributed by subsurface dynamics of the fumarole, they might also be associated with data quality. For instance, irregular and inconsistent sampling could significantly contribute to the fluctuation of peaks and troughs observed on time series plots. As stated in section 2.1.4, the sampling was inconsistently done (yearly basis), while data gaps were encountered in some cases. Since this is difficult to verify, interpretations were focused on the status of data and described as follows:

- The increase in the absolute composition of CO₂ and H₂S is associated with enhanced volcanic degassing activities in a geothermal system (Hunt, 2013). Such episodes directly result from enhanced boiling activities, which causes the escape of fumarole gases along vents in active, productive reservoirs (West jec, 2009), a situation evidenced by a rise in enthalpies of wells in the Olkaria East geothermal field (Wamalwa et al., 2016).
- The periods characterized by increased rapid fluctuations (spikes) are likely associated with subsurface hydrothermal unrest, typified by enhanced exhalation of gases underneath the geothermal system. Such events are usually linked with increased permeability of subsurface reservoir rocks, which can be attributed to increased pressure on reservoir rocks which enlarges the existing fractures and cracks on the host rocks (Eggertsson et al., 2020). It was not possible to establish this for this study due to the absence of literature on reservoir response studies.
- A decline in chloride concentration (e.g., in 2012) is due to the dilution of geothermal reservoir fluids resulting from the infiltration of meteoric fluids into the geothermal reservoir (Wamalwa et al., 2016). Other factors such as excessive injection of cold fluids have also been shown to decrease chloride concentration in geothermal systems (Hunt, 2013). In this study, the absence of well discharge chemistry data meant that it was impossible to associate such events to the dynamics of the geothermal reservoir and, to a large extent, the ‘geothermal motor.’
- The increase in absolute chloride levels (e.g., between 2012 to 2014) is caused by increased localized subsurface boiling (Karingithi, 2015). Such boiling mainly results from decreased pressure levels in the geothermal system (Wamalwa, 2017), which in the Olkaria context has been linked with the re-injection of hot fluids into the geothermal reservoir (Wafula, 2018). Such dynamics can be associated with a reduced speed of the geothermal motor.

4.6. Limitations of the study

The major limitation of the study was the absence of continuous TIR and geochemistry datasets. The data gaps between March and July 2019 for TIR datasets meant that the resulting temperature trend was not continuous, affecting subsequent analysis and interpretation. It also influenced the choice of time series normalization technique used.

Secondly, the unavailability of similar frequency secondary datasets made it impossible to compare geochemistry and temperature data's time series plot values. This meant that independent inference of subsurface conditions was made against the original goal of the study. In addition, irregular temporal frequency of gas geochemistry data limited the complete analysis and interpretation of the datasets.

Other factors such as wind speed, known to influence the surface's heat flux measurements, were not factored in the study. In addition, the study assumes uniform emissivity values of surface materials, thus makes the study's findings subjective.

5. CONCLUSIONS AND RECOMMENDATIONS

5.1. Conclusions

The research aimed to monitor fumarole activity using multi-temporal ground-based thermal infrared, meteorological, and gas discharge chemistry data. The following are the major conclusions in line with the study's objectives:

- The main environmental factors affecting the apparent radiant temperatures recorded by ground-based TIR cameras include rain, solar illumination, and fog. The TIR images acquired during foggy and rainy periods have lower radiant temperature values compared to those acquired during clear and sunny conditions. The surface factors affecting the apparent temperature mainly include material property and how they respond to various under different meteorological conditions. In this study, the surface influences were more pronounced in the thermally anomalous region of interest, near the fumarole area than in other background regions, composed of vegetation, unconsolidated pyroclastic rubble.
- The standard deviation of radiant temperature of TIR images pixels is useful in identifying and isolating images acquired under different weather conditions. In this study, the images acquired during foggy or rainy conditions had lower standard deviation values than those collected during sunny and clear conditions. The effectiveness of using this index for thresholding is dependent on the hour of acquisition. For this study, higher accuracy of isolation was attained on night-time acquisitions compared to daytime scenes.
- Time series plots of apparent radiant temperature values of regions of specific hour-of-day images show variation with seasonality. The seasonal variation is due to the influence of meteorological-induced factors such as rain, fog, and solar illumination on the apparent radiant temperature values. The variation is ROI-specific and is most pronounced on the hottest regions of area of focus (i.e., ROI-1). The study found that night-time data suffers from the effects of fog, while day-time data from seasonality induced by solar illumination effects.
- Time series normalization (using the background removal procedure) is an effective technique of isolating signals associated with meteorological induced influences such as fog. However, the success of this procedure relies on hour of acquisition of the TIR scenes; with higher accuracy attained on night-time scenes. Applying the normalization on time series plots did not affect the overall trend pattern, but removed the extremely low values (troughs) from the time series plots. It is therefore concluded that night-time data can be corrected by the algorithm compared to daytime data.
- Heat flux time-series plots (calculated from normalized time series values) effectively affect surface emitted radiance estimation. The trends compare with those of detrended temperature plots of various ROIs, illustrating its dependence on the recorded apparent radiant temperature. Despite this similarity, heat flux

plots give an impression of subsurface emission, characteristic of geothermal fields. As such, it can be concluded that periods characterized by increasing heat flux trends are associated with the agitation of subsurface hydrothermal fluids, interpreted to be associated with the increased speed of the geothermal motor. The periods characterized by constant trends generally describe quiescent periods of the geothermal reservoir, an indication of reduced geothermal motor speed..

- The time series plots of absolute chemical concentration of specific fumarole components (e.g., CO₂, H₂S, and Cl) show variability in trends, with occasional spikes on specific periods of observation. Periods characterized by increased CO₂ and H₂S are generally associated with increased emission of gases from the subsurface reservoir onto the fumarole vent, which is linked with enhanced subsurface degassing. For this study, such behaviour is associated with increased boiling activities, an implication of increased geothermal activities, which can be attributed to increased speed of geothermal motor. On the other hand, periods with increased chloride content are generally characterized by dilution of chloride fluids, by subsurface steam-heated fluids. For this study, it is concluded that such behaviour results from increased subsurface reservoir, associated with an increased in geothermal motor speed.

5.2. Recommendations

The following recommendations are made based on interpretation of this study's findings and conclusions:

- Incorporate downhole data of wells within the Ololbutot fault axis further to understand the subsurface dynamic of the geothermal reservoir. It would be interesting to monitor how their flow rates, pressure/temperature, and enthalpies change with time; and establish how their trends compare with radiant temperature measurements of OMF8.
- The use of continuous time series TIR datasets to address gaps brought about by data gaps and test other time series normalization techniques. For instance, the periods of incomplete datasets (i.e., March-July 2020) fall during prolonged precipitation (long-rains), implying that it was impossible to investigate their effects on both apparent radiant temperature and estimated heat flux.
- Regular and consistent sampling of fumarole gas discharge data to compare with radiant temperature measurements, collected by TIR images. In addition, incorporate other anions and cation components of fumarole gas discharge (e.g., Na, Ca, Mg²⁺, etc.) to understand other processes, e.g., mixing of surface fluids that characterizes the behavior of geothermal reservoirs.

LIST OF REFERENCES

- (West jec), W. J. E. C. I. (2009). *The Olkaria Optimization Study (Phase II)—Final Reservoir Analysis Report*. Retrieved from <http://www.wjec.co.jp>
- Arnórsson, S., Bjarnason, J. Ö., Giroud, N., Gunnarsson, I., & Stefánsson, A. (2006). Sampling and analysis of geothermal fluids. *Geofluids*, 6(3), 203–216. <https://doi.org/10.1111/j.1468-8123.2006.00147.x>
- Axelsson, G. (2010). Sustainable geothermal utilization - Case histories; definitions; research issues and modelling. *Geothermics*, 39(4), 283–291. <https://doi.org/10.1016/j.geothermics.2010.08.001>
- Axelsson, G., Arnaldsson, A., Mortensen, A., Bore, C., Karingithi, C., Koech, V., ... Engineers, V. C. (2013). CONCEPTUAL MODEL AND RESOURCE ASSESSMENT FOR THE OLKARIA GEOTHERMAL SYSTEM, KENYA Gudni. *Short Course V on Conceptual Modelling of Geothermal Systems*, 1–21. Reykjavík: United Nations University, GTP.
- Balamuralidhar, N., Tilon, S., & Nex, F. (2021). MultEYE: Monitoring system for real-time vehicle detection, tracking and speed estimation from UAV imagery on edge-computing platforms. *Remote Sensing*, 13(4), 1–24. <https://doi.org/10.3390/rs13040573>
- Barrick, K. A. (2007). Geyser decline and extinction in New Zealand-energy development impacts and implications for environmental management. *Environmental Management*. <https://doi.org/10.1007/s00267-005-0195-1>
- Bülbül, A. (2015). Mixing of geothermal and non-geothermal fluids in shallow aquifers in the Germencik-Nazilli area, Büyük Menderes Basin (SW Turkey). *Geodinamica Acta*, 27(1), 67–81. <https://doi.org/10.1080/09853111.2014.979529>
- Chan, H. P., & Chang, C. P. (2018). Exploring and monitoring geothermal and volcanic activity using Satellite Thermal Infrared data in TVG, Taiwan. *Terrestrial, Atmospheric and Oceanic Sciences*, 29(4), 387–404. <https://doi.org/10.3319/TAO.2018.01.22.01>
- Chiodini, G., Vilardo, G., Augusti, V., Granieri, D., Caliro, S., Minopoli, C., & Terranova, C. (2007). Thermal monitoring of hydrothermal activity by permanent infrared automatic stations: Results obtained at Solfatara di Pozzuoli, Campi Flegrei (Italy). *Journal of Geophysical Research: Solid Earth*, 112(12), 1–13. <https://doi.org/10.1029/2007JB005140>
- Cleveland, R.B., Cleveland, W.S., McRae, J.E., Terpenning, I. J., Eaquinca, J. R. R., & Medinilla, E. E. (1990). STL: A Seasonal-Trend Decomposition Procedure based on LOESS. *Journal of Official Statistics*, 6(1), 3–73. Retrieved from <http://www.ncbi.nlm.nih.gov/pubmed/2207653>
- Coolbaugh, M., & Sladek, C. (2013). Measurement of heat loss associated with shallow thermal aquifers in Nevada, USA. *Transactions - Geothermal Resources Council*, 37(PART 1), 249–254.
- Dawson, G. B., & Dickinson, D. J. (1970). Heat flow studies in thermal areas of the North Island of New Zealand. *Geothermics*, 2(PART 1), 466–473. [https://doi.org/10.1016/0375-6505\(70\)90045-3](https://doi.org/10.1016/0375-6505(70)90045-3)
- Diaz, R. A., Eylem, K., & Zarrouk, S. J. (2016). Reinjection in geothermal fields - A worldwide review update. *Renewable and Sustainable Energy Reviews*, 53, 105–162. <https://doi.org/10.1016/j.rser.2015.07.151>
- Eggertsson, G. H., Lavallée, Y., Kendrick, J. E., & Markússon, S. H. (2020). Improving fluid flow in geothermal reservoirs by thermal and mechanical stimulation: The case of Krafla volcano, Iceland. *Journal of Volcanology and Geothermal Research*, 391, 106351. <https://doi.org/10.1016/j.jvolgeores.2018.04.008>
- ESRI. (2021). World Topographic Map. Retrieved July 15, 2021, from Esri website: https://services.arcgisonline.com/ArcGIS/rest/services/World_Topo_Map/MapServer
- Fadel, I., C. Hecker, J. Kimata, E. Bonyo, M. van der Meijde, H. van der Werff, and F. van der M. (2021). Geoscientific Monitoring of Olkaria's Geothermal Motor. *EOS*, 102. <https://doi.org/https://doi.org/10.1029/2021EO153904>
- FLIR. (2021). Teledyne FLIR. Retrieved July 8, 2021, from <https://www.flir.eu/products/a655sc/>
- Gaudin, D., Tullio, R., Finizola, A., Delcher, E., Salvatore, A., Barde-Cabusson, S., ... Vita, F. (2017). Heat flux-based strategies for the thermal monitoring of sub-fumarolic areas: Examples from Vulcano and La Soufrière de Guadeloupe. *Journal of Volcanology and Geothermal Research*, 343, 122–134. <https://doi.org/10.1016/j.jvolgeores.2017.06.021>
- Haselwimmer, C., Prakash, A., & Holdmann, G. (2013). Quantifying the heat flux and outflow rate of hot springs using airborne thermal imagery: Case study from Pilgrim Hot Springs, Alaska. *Remote Sensing of Environment*, 136, 37–46. <https://doi.org/10.1016/j.rse.2013.04.008>
- Hedenquist, J. W. (1991). Boiling and dilution in the shallow portion of the Waiotapu geothermal system, New Zealand. *Geochimica et Cosmochimica Acta*, 55(10), 2753–2765. [https://doi.org/10.1016/0016-7037\(91\)90442-](https://doi.org/10.1016/0016-7037(91)90442-)

- Hunt, M. T. (2013). Geothermal Field and Reservoir Monitoring. In *Encyclopedia of Sustainability Science and Technology* (pp. 4203–4230). https://doi.org/https://doi.org/10.1007/978-1-4419-0851-3_298
- Ingebritsen, S. E., & Mariner, R. H. (2010). Hydrothermal heat discharge in the Cascade Range, northwestern United States. *Journal of Volcanology and Geothermal Research*, 196(3–4), 208–218. <https://doi.org/10.1016/j.jvolgeores.2010.07.023>
- Inguaggiato, S., Diliberto, I. S., Federico, C., Paonita, A., & Vita, F. (2018). Review of the evolution of geochemical monitoring, networks and methodologies applied to the volcanoes of the Aeolian Arc (Italy). *Earth-Science Reviews*, 176(September 2017), 241–276. <https://doi.org/10.1016/j.earscirev.2017.09.006>
- Karingithi, C. W. (2015). the Geochemical Reservoir Monitoring - a Case Study of Olkaria Northeast Field in Kenya. In UNU-GTP (Ed.), *Short Course VIII on Exploration for Geothermal Resource* (Vol. 204, pp. 1–16). Retrieved from <https://orkustofnun.is/gogn/unu-gtp-sc/UNU-GTP-SC-21-0604B.pdf>
- Koech, V. K. (2014). *Numerical Geothermal Reservoir Modelling and Infield Reinjection Design, Constrained by Tracer Test Data: Case Study for the Olkaria Geothermal Field in Kenya* (University of Iceland). Retrieved from <https://orkustofnun.is/gogn/unu-gtp-report/UNU-GTP-2014-05.pdf>
- Kou, Y., Lu, C. T., & Chen, B. (2006). Spatial weighted outlier detection. *Proceedings of the Sixth SIAM International Conference on Data Mining*, 1, 614–618. <https://doi.org/10.1137/1.9781611972764.71>
- Kuenzer, C., & Dech, S. (2013). Remote Sensing and Digital Image Processing Thermal Infrared Remote Sensing. In F. D. Van Der Meer (Ed.), *Remote Sensing and Digital Image Processing*. https://doi.org/DOI10.1007/978-94-007-6639-6_1
- Lagat, J. (2007). Hydrothermal alteration mineralogy in geothermal fields with case examples from Olkaria domes geothermal field, Kenya. *Short Course II on Surface Exploration for Geothermal ...*, 1–24. Retrieved from <http://www.os.is/gogn/unu-gtp-sc/UNU-GTP-SC-05-10.pdf>
- Lillesand, R.W., Kiefer R.W., C. J. W. (2008). *Remote Sensing and Image Interpretation* (6th ed.). New York: Wiley & Sons, Inc.
- Lindsey, C., Lubenow, B., Fairley, J., & Larson, P. (2015). Ice box calorimetry: A test of applicability in non-steaming geothermal areas. *Transactions - Geothermal Resources Council*, 39(October 2015), 421–423.
- Lund, J. W. (2013). Geothermal Energy Utilization. In *Renewable Energy Systems* (pp. 4162–4800). https://doi.org/https://doi.org/10.1007/978-1-4614-5820-3_231
- Malvina, S., Rabuffi, F., Pisciotta, A., Musacchio, M., Diliberto, I. S., Spinetti, C., ... Buongiorno, M. F. (2019). Analysis of thermal anomalies in volcanic areas using multiscale and multitemporal monitoring: Vulcano Island test case. *Remote Sensing*, 11(2). <https://doi.org/10.3390/rs11020134>
- Meyers, A. R. (2012). Encyclopedia of Sustainability Science and Technology. In *Encyclopedia of Sustainability Science and Technology*. <https://doi.org/10.1007/978-1-4419-0851-3>
- Mia, M. B., Bromley, C. J., & Fujimitsu, Y. (2012). Monitoring heat flux using Landsat TM/ETM+ thermal infrared data - A case study at Karapiti ('Craters of the Moon') thermal area, New Zealand. *Journal of Volcanology and Geothermal Research*, 235–236, 1–10. <https://doi.org/10.1016/j.jvolgeores.2012.05.005>
- Munyiri, S. K. (2016). Structural Mapping of Olkaria Domes Geothermal Field Using Geochemical Soil Gas Surveys , Remote Sensing and Gis (Vol. 7). United Nations University.
- Njoroge, D. W. (2016). *Monitoring and Evaluation Framework for Geothermal Projects: Olkaria I Unit 6, Kenya* (Vol. 2030). Retrieved from <https://orkustofnun.is/gogn/unu-gtp-report/UNU-GTP-2016-28.pdf>
- Ofwona, C. O. (2002). *A Reservoir Study of Olkaria East Geothermal System, Kenya*. Retrieved from <http://www.unugtp.is/en/moya/page/p2002/>
- Omenda, P. (2018). Geothermal Outlook in East Africa: Perspectives for Geothermal Development Irena-IGA presentation. *International Geothermal Association*, (31). Retrieved from <https://www.irena.org/-/media/Files/IRENA/Agency/Events/2018/Jan/Geothermal-financing/S1-p1-IRENA-IGA-Presentation-31-01-2018.pdf?la=en&hash=52618994FFFF6833CFF3B51C6199982BC042741C>
- Onacha, S.A., Mungania, J. (1993). Surface Exploration of Domes Area : an Extension of Olkaria Geothermal Field. *Proceedings 15thNZ Geothermal Workshop 1993*, 93–98. Retrieved from <https://pangea.stanford.edu/ERE/pdf/IGASstandard/NZGW/1993/Onacha.pdf>
- Ouma, P., Koech, V., & Mwarania, F. (2016). *Olkaria Geothermal Field Reservoir Response After 35 Years of Production (1981 – 2016)*. 6(November), 1–13. Retrieved from [http://theargo.org/fullpapers/Olkaria Geothermal Field reservoir response after 35 years of production.pdf](http://theargo.org/fullpapers/Olkaria%20Geothermal%20Field%20reservoir%20response%20after%2035%20years%20of%20production.pdf)
- Ozawa, Y. (1958). Some Observations of the Heat Balance on the Ground Surface. *Journal of Agricultural Meteorology*, 13(4), 135–139. <https://doi.org/10.2480/agrmet.13.135>
- Pavlidou, E., van der Meijde, M., van der Werff, H., & Hecker, C. (2016). Finding a needle by removing the haystack: A spatio-temporal normalization method for geophysical data. *Computers and Geosciences*, 90, 78–86.

<https://doi.org/10.1016/j.cageo.2016.02.016>

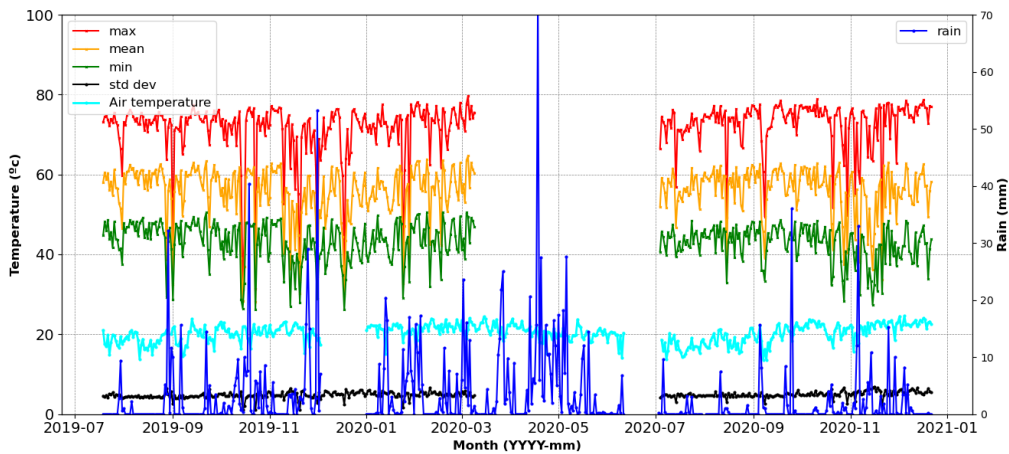
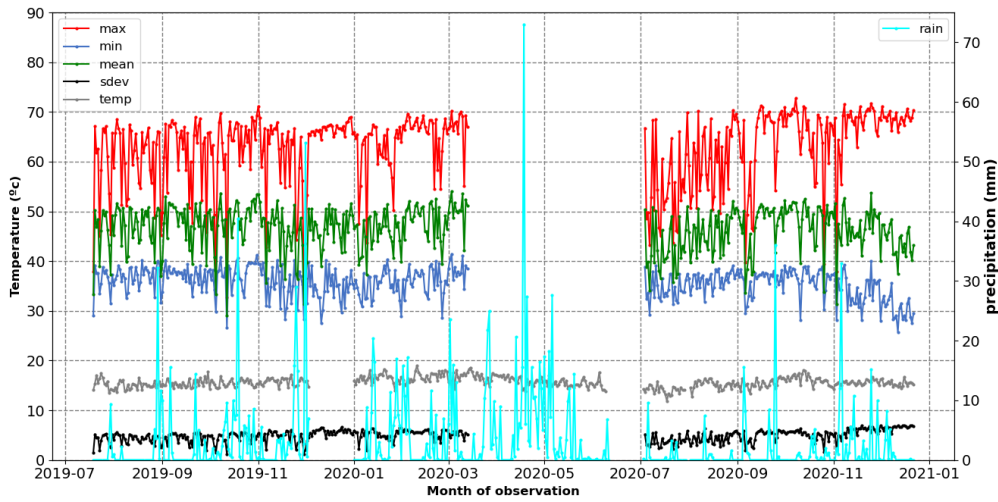
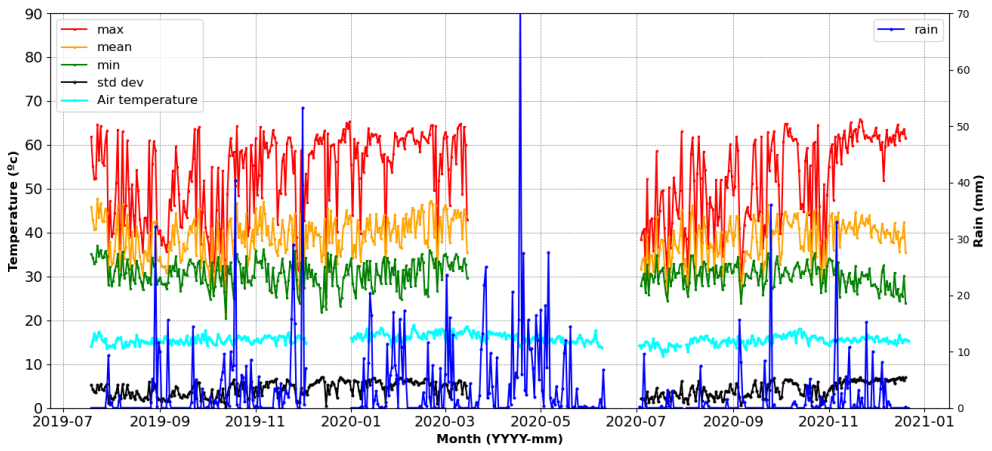
- Rashmin, C. G., Foulger, G. R., & Julian, B. R. (2003). Reservoir depletion at The Geysers geothermal area, California, shown by four-dimensional seismic tomography. *Journal of Geophysical Research: Solid Earth*, 108(B3), 1–11. <https://doi.org/10.1029/2001jb000638>
- Romaguera, M., Vaughan, R. G., Ettema, J., Izquierdo-Verdiguier, E., Hecker, C. A., & van der Meer, F. D. (2018). Detecting geothermal anomalies and evaluating LST geothermal component by combining thermal remote sensing time series and land surface model data. *Remote Sensing of Environment*, 204(September 2017), 534–552. <https://doi.org/10.1016/j.rse.2017.10.003>
- Sansivero, F., Scarpato, G., & Vilardo, G. (2013). The automated infrared thermal imaging system for the continuous long-term monitoring of the surface temperature of the Vesuvius crater. *Annals of Geophysics*, 56(4), 1–10. <https://doi.org/10.4401/ag-6460>
- Sansivero, F., & Vilardo, G. (2019). Processing thermal infrared imagery time-series from volcano permanent ground-based monitoring network. Latest methodological improvements to characterize surface temperatures behavior of thermal anomaly areas. *Remote Sensing*, 11(5). <https://doi.org/10.3390/rs11050553>
- Silvestri, M., Marotta, E., Buongiorno, M. F., Avvisati, G., Belviso, P., Sessa, E. B., ... Teggi, S. (2020). Monitoring of surface temperature on parco delle biancane (Italian geothermal area) using optical satellite data, UAV and field campaigns. *Remote Sensing*, 12(12). <https://doi.org/10.3390/rs12122018>
- Spampinato, L., Oppenheimer, C., Cannata, A., Montalto, P., Salerno, G. G., & Calvari, S. (2012). On the time-scale of thermal cycles associated with open-vent degassing. *Bulletin of Volcanology*, 74(6), 1281–1292. <https://doi.org/10.1007/s00445-012-0592-2>
- Stevenson, J. A., & Varley, N. (2008). Fumarole monitoring with a handheld infrared camera: Volcán de Colima, Mexico, 2006-2007. *Journal of Volcanology and Geothermal Research*, 177(4), 911–924. <https://doi.org/10.1016/j.jvolgeores.2008.07.003>
- Treiman, A. H., & Filiberto, J.V., Kaaden, K. E. (2021). Near-infrared Reflectance of Rocks at High Temperature: Preliminary Results and Implications for Near-infrared Emissivity of Venus's Surface. *The Planetary Science Journal*, 2(2), 43. <https://doi.org/10.3847/psj/abd546>
- Vaughan, R. G., Keszthelyi, L. P., Lowenstern, J. B., Jaworowski, C., & Heasler, H. (2012). Use of ASTER and MODIS thermal infrared data to quantify heat flow and hydrothermal change at Yellowstone National Park. *Journal of Volcanology and Geothermal Research*. <https://doi.org/10.1016/j.jvolgeores.2012.04.022>
- Wafula, E. (2018). Geochemical changes and processes in the Olkaria East Reservoir 1984 to 2017. *Proceedings, 7th African Rift Geothermal Conference*, (November). Retrieved from [http://theargeo.org/fullpapers/C7/Geochemical changes and processes in the Olkaria East Reservoir-converted.pdf](http://theargeo.org/fullpapers/C7/Geochemical%20changes%20and%20processes%20in%20the%20Olkaria%20East%20Reservoir%20converted.pdf)
- Wamalwa, R. N. (2017). *Evaluation of the Geothermal Energy Potential of the Olkaria Field Kenya, Based On Geochemical Data-A Numerical Model* (University of Nairobi). Retrieved from <https://pdfs.semanticscholar.org/b8db/59399e068ec5eb79b1b22f055494b22dda2f.pdf>
- Wamalwa, R. N., Nyamai, C. M., Ambusso, W. J., Mulwa, J., & Waswa, A. K. (2016). Structural Controls on the Geochemistry and Output of the Wells in the Olkaria Geothermal Field of the Kenyan Rift Valley. *International Journal of Geosciences*, 07(11), 1299–1309. <https://doi.org/10.4236/ijg.2016.711094>
- Wen, H. Y., Yang, T. F., Lan, T. F., Lee, H. F., Lin, C. H., Sano, Y., & Chen, C. H. (2016). Soil CO₂ flux in hydrothermal areas of the Tatun Volcano Group, Northern Taiwan. *Journal of Volcanology and Geothermal Research*, 321, 114–124. <https://doi.org/10.1016/j.jvolgeores.2016.04.021>
- Zimmer, M., Walter, T. R., Kujawa, C., Gaete, A., & Franco-Marin, L. (2017). Thermal and gas dynamic investigations at Lastarria volcano, Northern Chile. The influence of precipitation and atmospheric pressure on the fumarole temperature and the gas velocity. *Journal of Volcanology and Geothermal Research*, 346, 134–140. <https://doi.org/10.1016/j.jvolgeores.2017.03.013>

6. APPENDICES

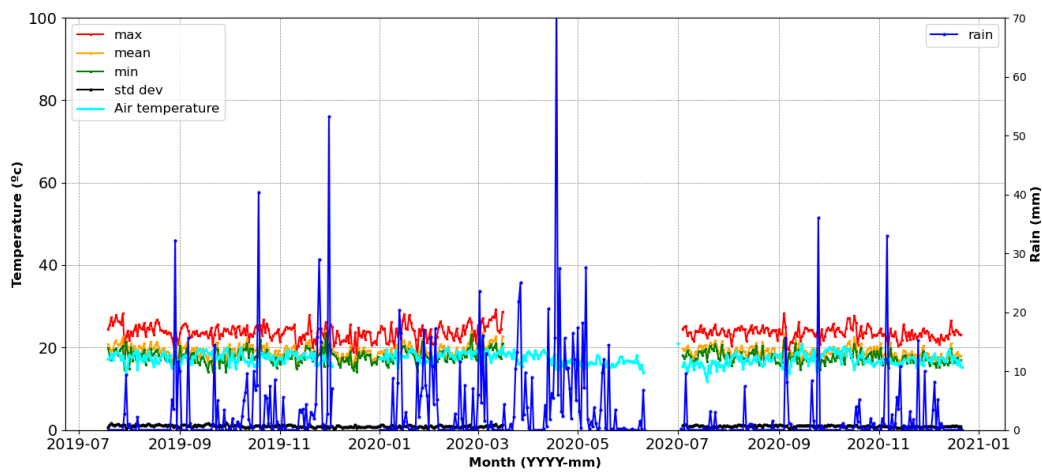
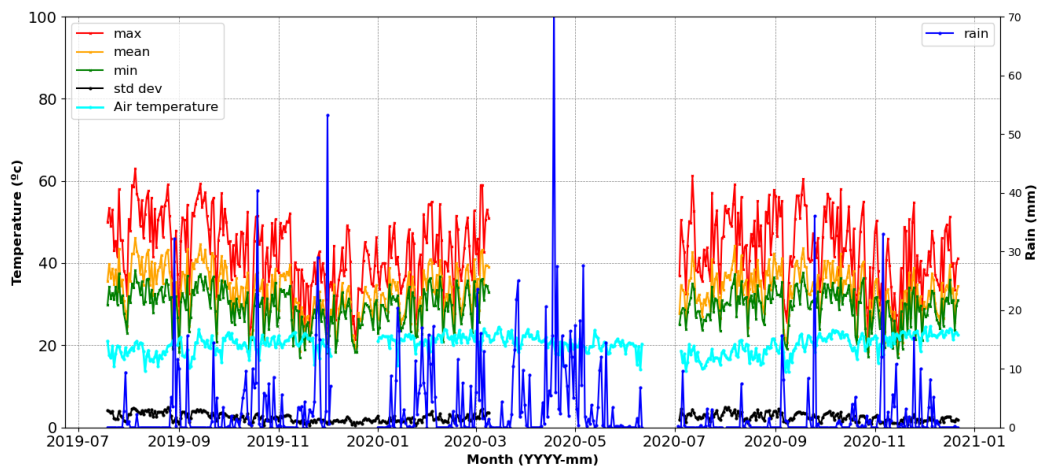
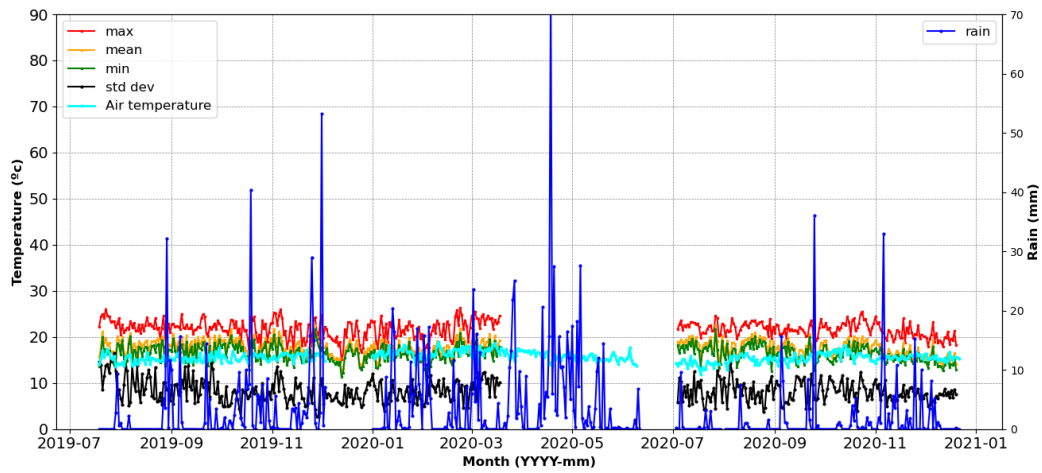
Appendix 1: Principal component matrix showing contribution of the first five components of ROI-1

HOUR	PRINCIPAL COMPONENT	VARIANCE CONTRIBUTION (%)	ACCUMULATIVE OF EIGENVALUES
00:00 UTC	PC1	94.02465666	94.02465666
	PC2	4.703103747	98.72776041
	PC3	0.782166582	99.50992699
	PC4	0.280347842	99.79027483
	PC5	0.209725168	100
03:00 UTC	PC1	93.88727245	93.88727245
	PC2	4.574984375	98.46225683
	PC3	0.919565574	99.3818224
	PC4	0.367348124	99.74917052
	PC5	0.250829477	100
09:00 UTC	PC1	96.25708975	96.25708975
	PC2	2.037961964	98.29505172
	PC3	1.29714507	99.59219679
	PC4	0.215624261	99.80782105
	PC5	0.192178952	100
12:00 UTC	PC1	95.94027934	95.94027934
	PC2	2.175986074	98.11626541
	PC3	1.379883134	99.49614855
	PC4	0.281103914	99.77725246
	PC5	0.222747539	100
21:00 UTC	PC1	94.98272944	94.98272944
	PC2	3.85043995	98.83316939
	PC3	0.662584063	99.49575346
	PC4	0.29075348	99.78650693
	PC5	0.213493065	100

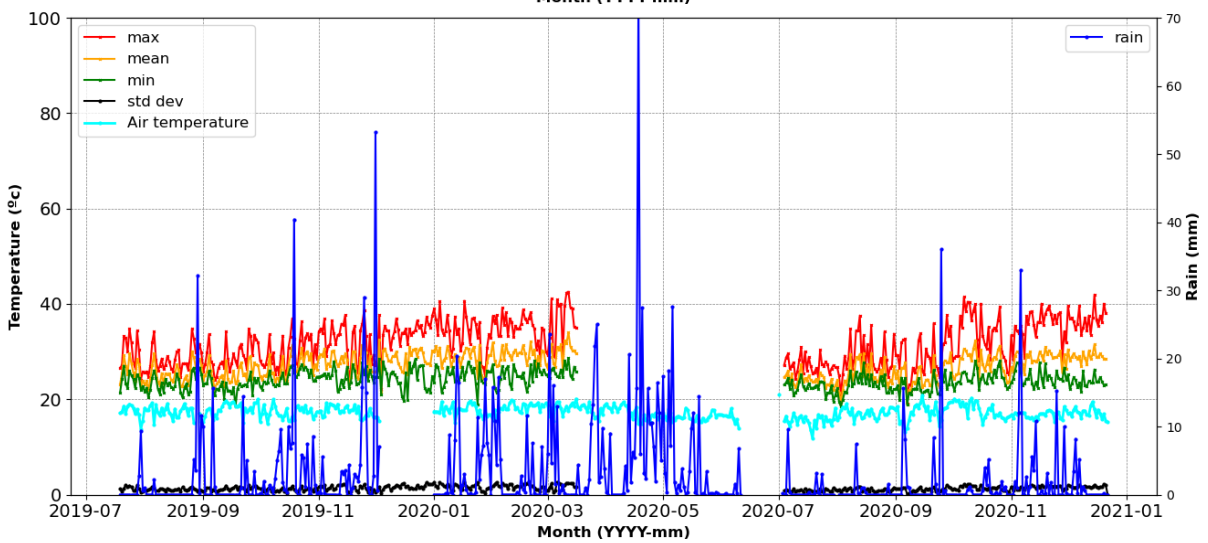
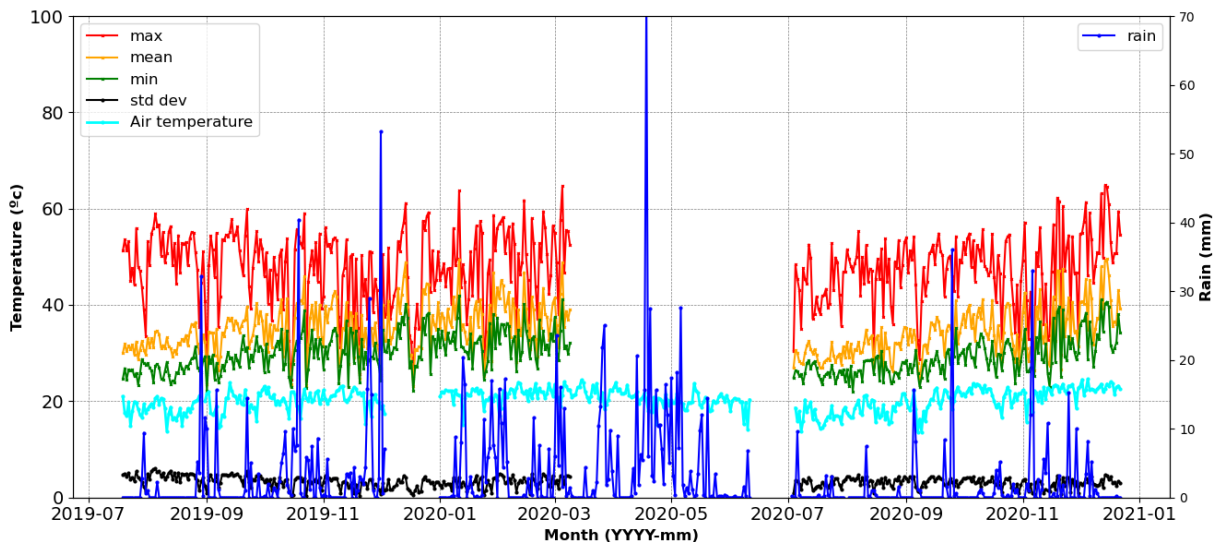
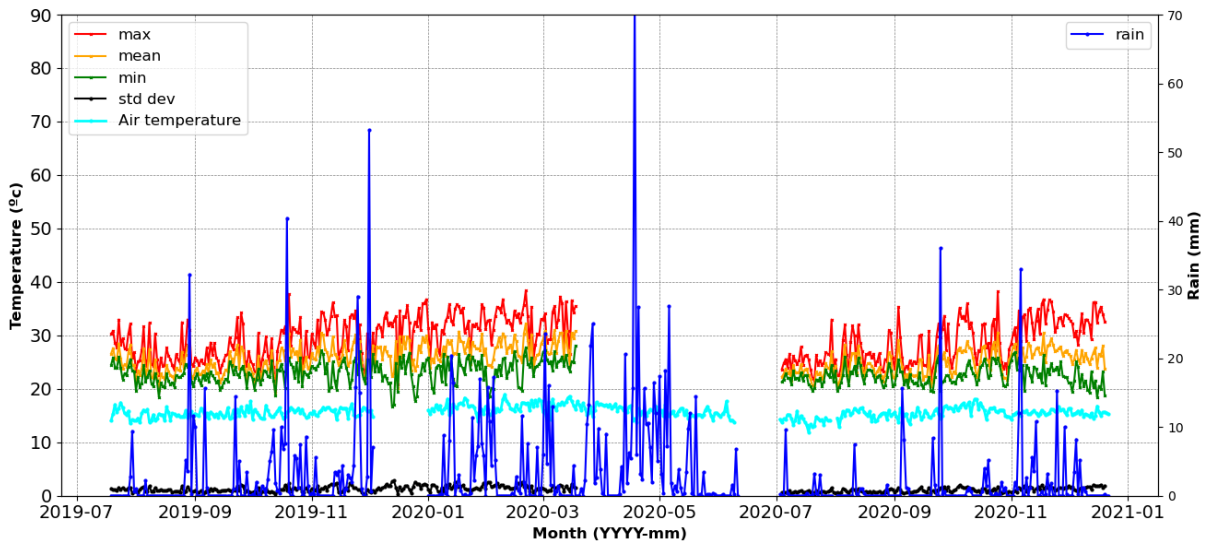
Appendix 2: Time series plots of radiant temperature values of ROI-1 (03:00 UTC, 06:00 UTC, and 12:00 UTC



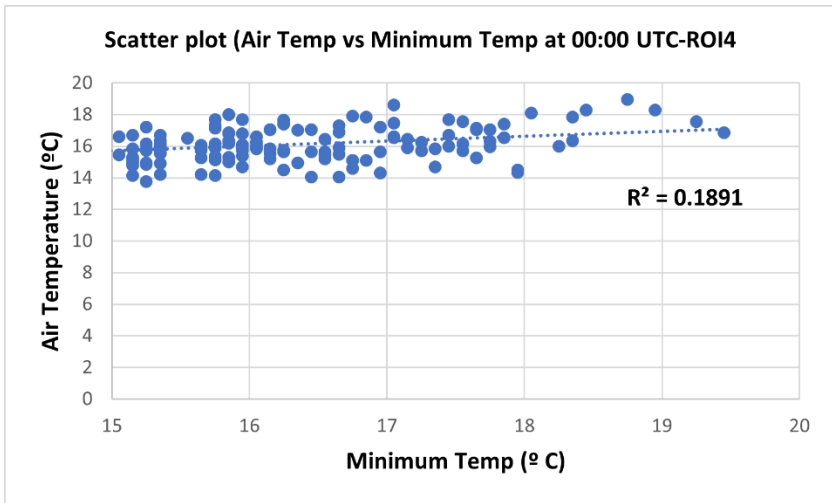
Appendix 3: Time series plots of radiant temperature values of ROI-2 (03:00 UTC, 06:00 UTC, and 12:00 UTC)



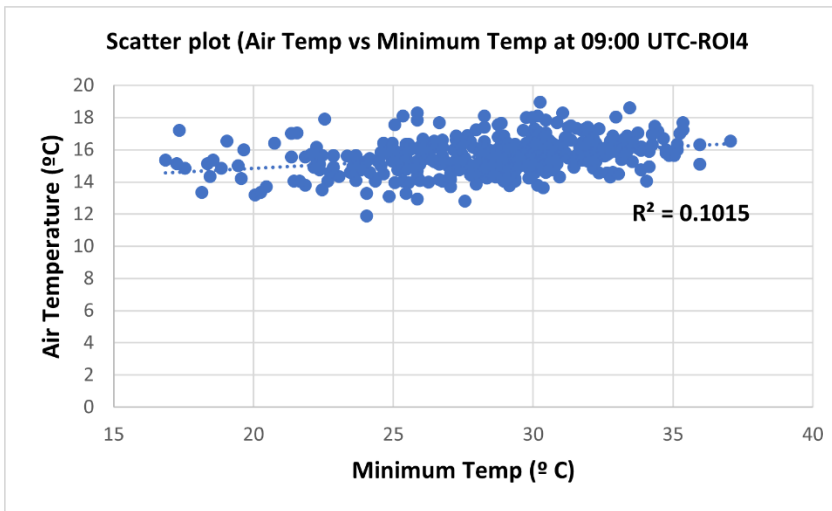
Appendix 4: Time series plots of radiant temperature values of ROI-2 (03:00 UTC, 06:00 UTC, and 12:00 UTC)



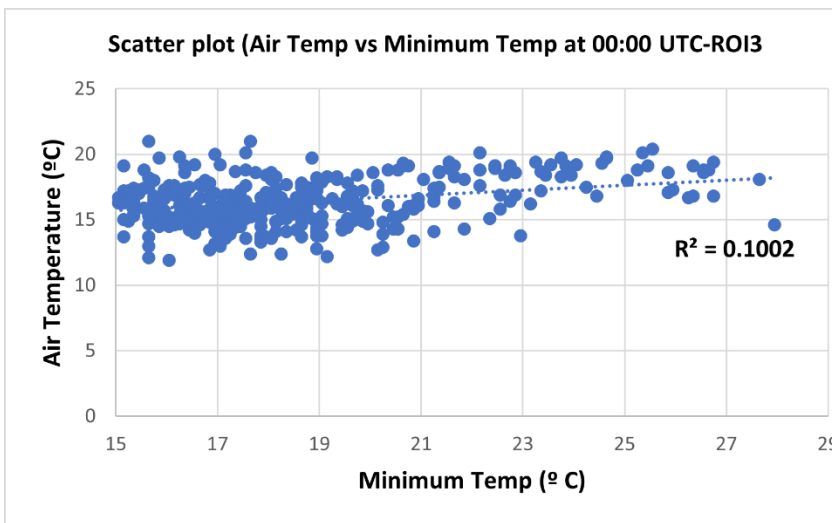
Appendix 5: Scatter plots showing the relationship between minimum radiant temperature values and air temperature



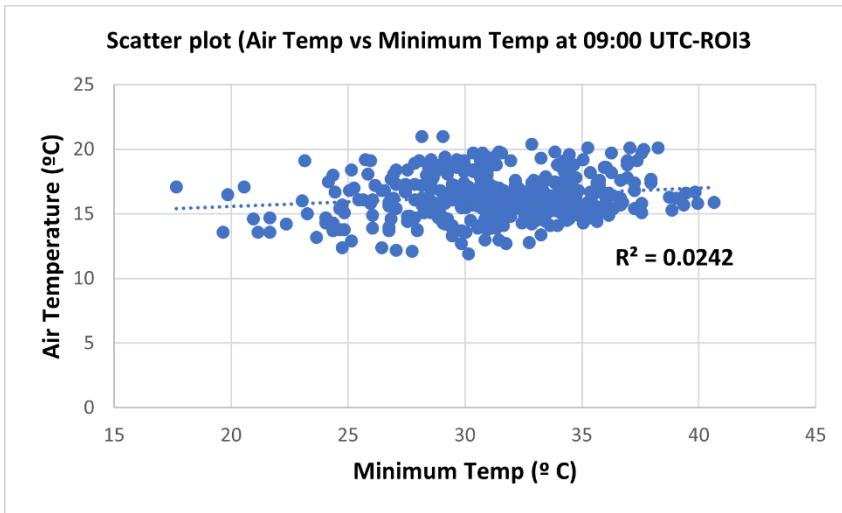
(i)



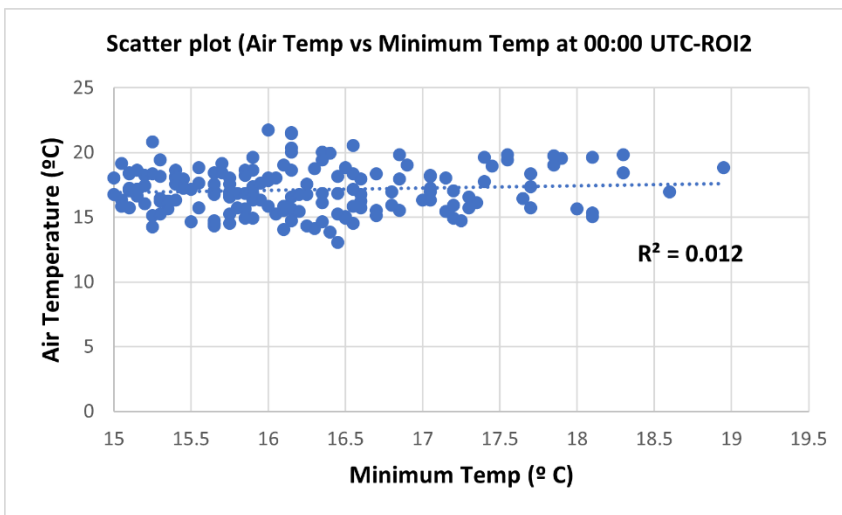
(ii)



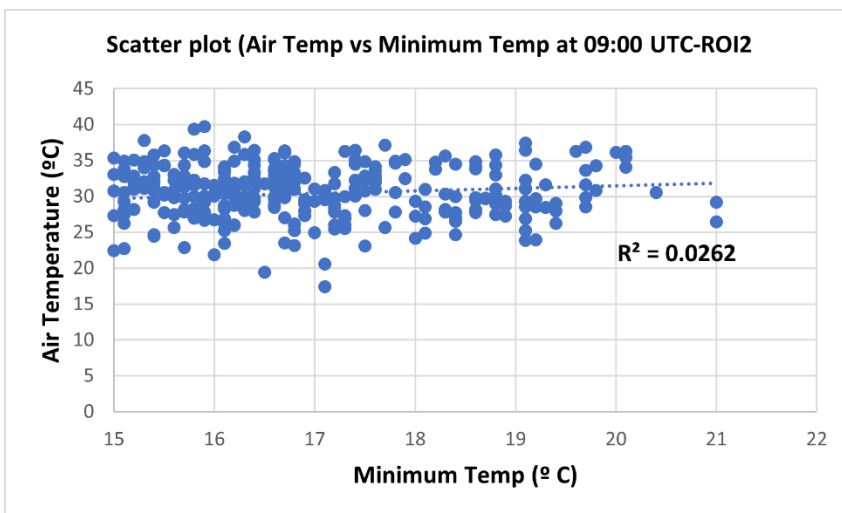
(iii)



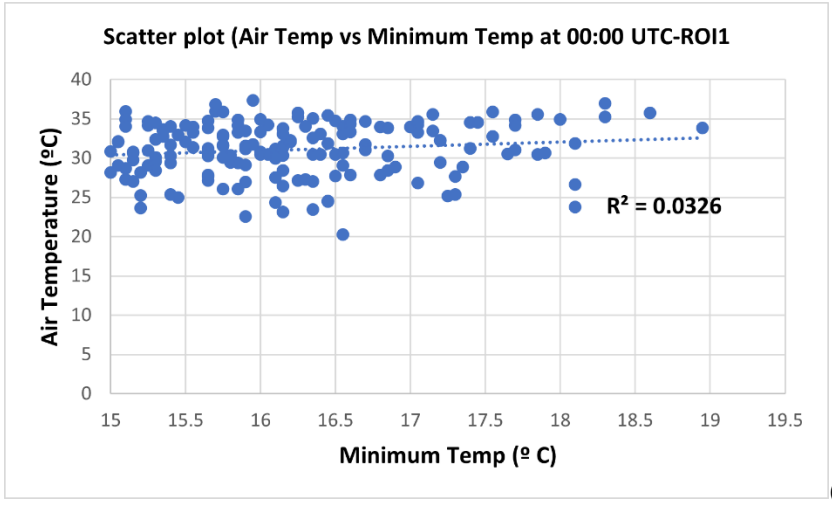
(iv)



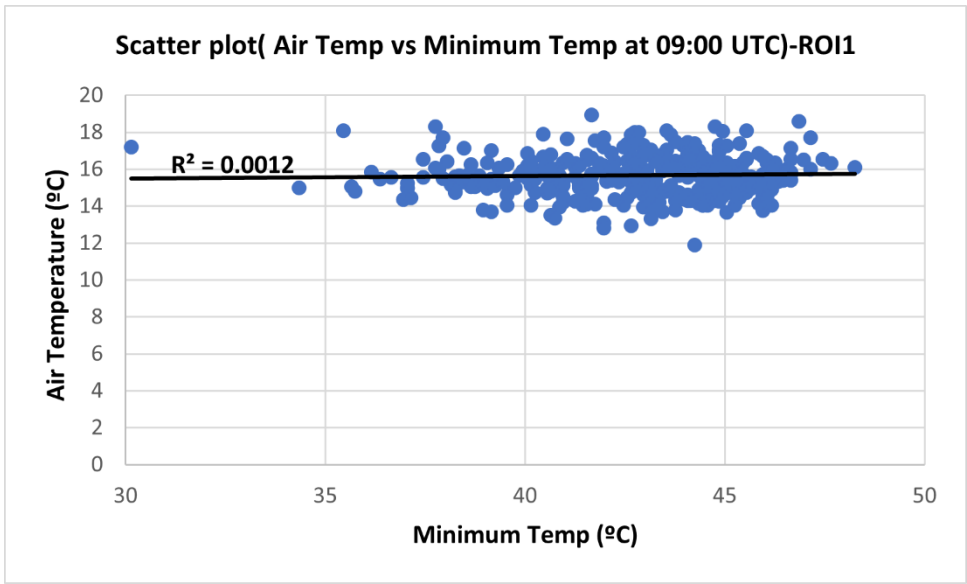
(v)



(vi)

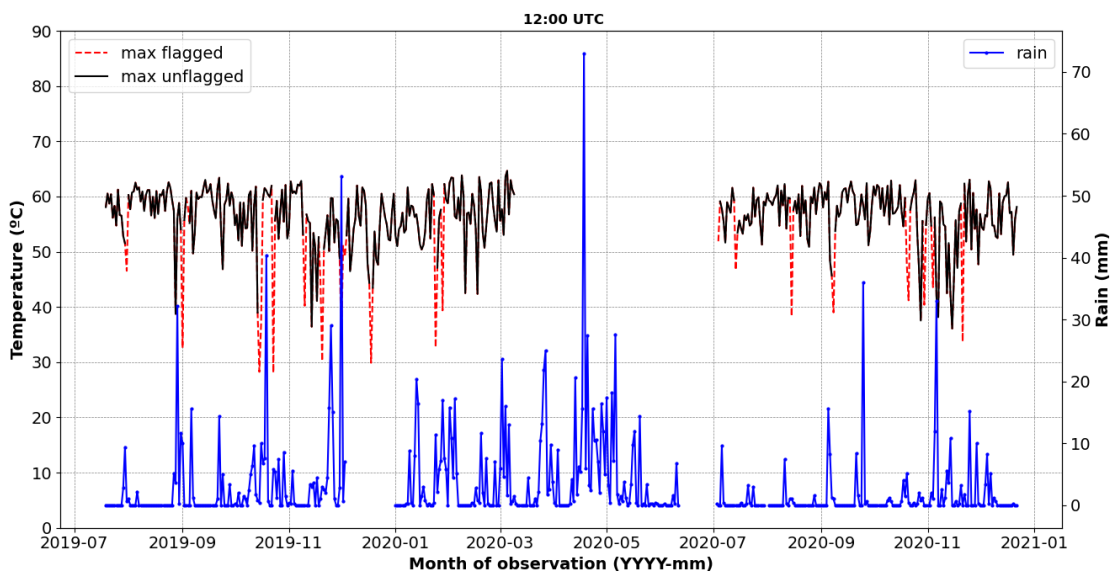
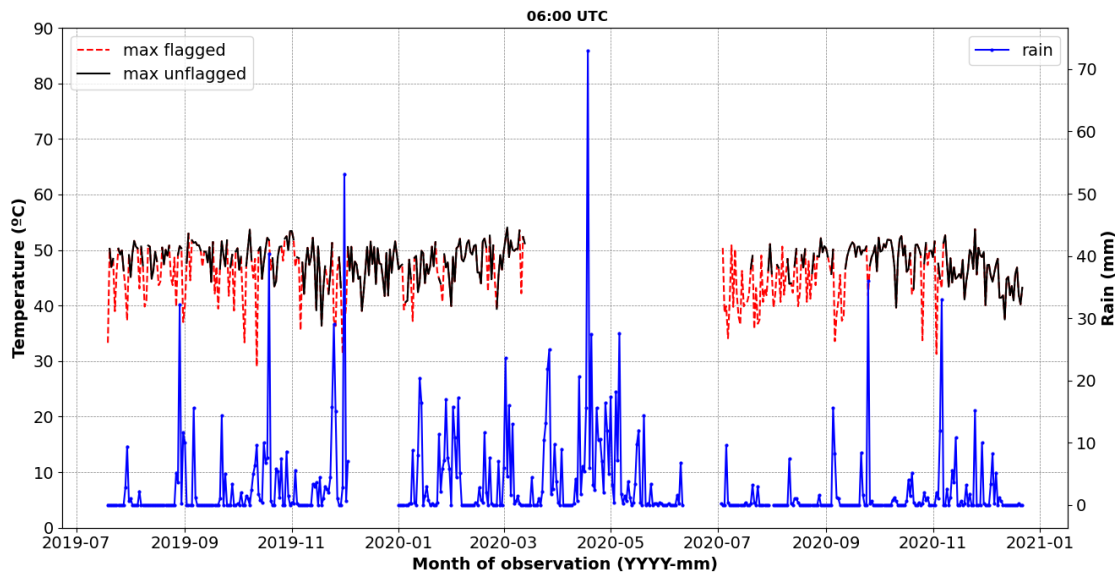
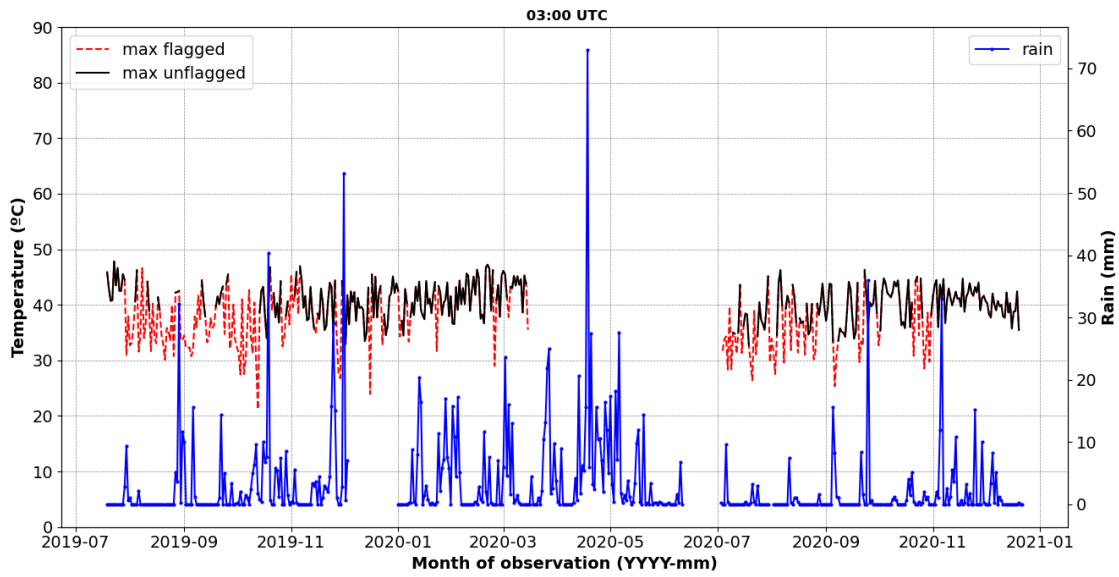


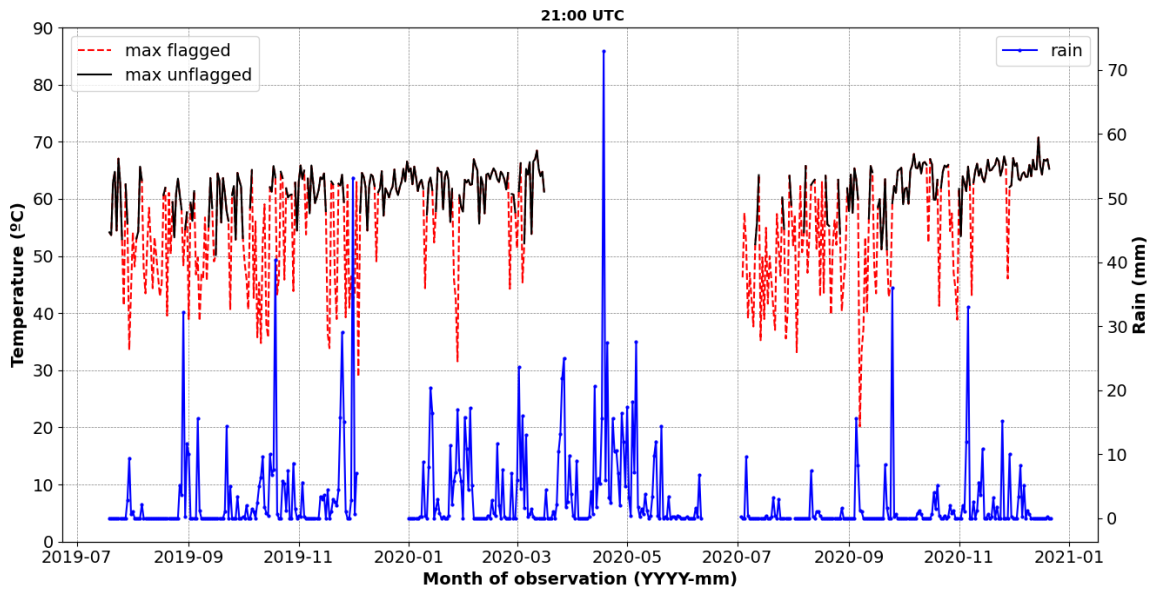
(vii)



(viii)

Appendix 6: Fog removed radiant temperature time series plots

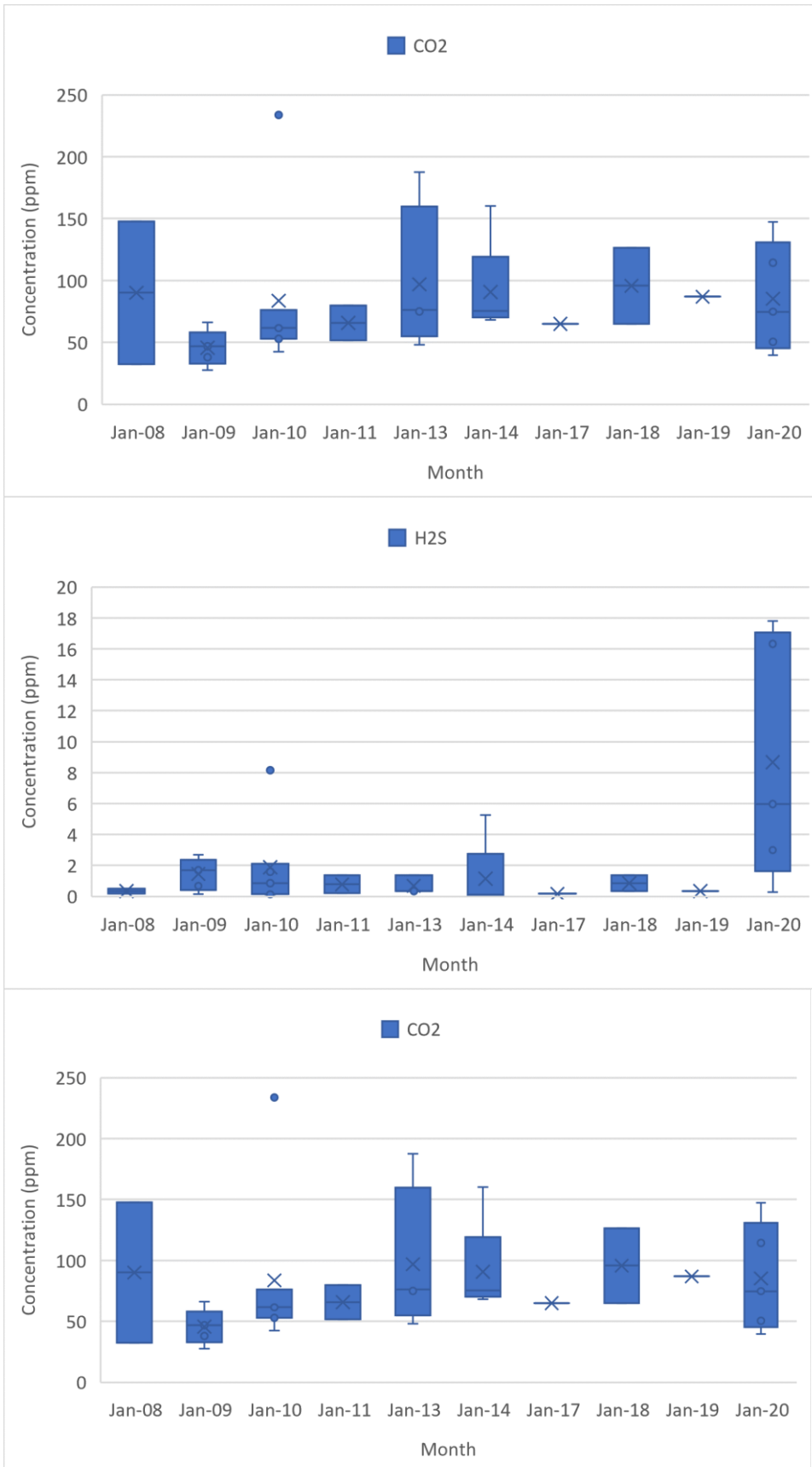




Appendix 7: Fumarole gas chemical concentration of OMF-8

Date	SO4	Cl (ppm)	CO ₂	H ₂ S	SiO ₂ (ppm)	Ca (ppm)	Li(ppm)	Na (ppm)
07/02/2008	30.7	0.5	32.45	0.17		0.791	0	0.491
10/11/2008	21.4		147.75	0.51	8.38	0.008	0.105	15.05
07/04/2009	11.9	0.375	27.72	0.68	0.01	0.62*	0	2.07
30/07/2009	2.5	0.15	38.06	0.136	0.3	1.37	0.001	0.79
11/11/2009	11.7	0	66	2.04	0.39	1.616	0	0.77
26/11/2009	28.3	7.56	49.94	2.686	0.5	2.224	0.002	0.94
08/10/2009	7.5	0	46.86	1.7	0.275	1.246	0	0
22/01/2010	28.6	0.41	76.12	1.6	0.425	0.34	0	0.516
17/02/2010	30.1	0.0625	61.6	2.11	0.3	0.157	0	0.409
17/03/2010	26.8	0.4	53.02	0.85	0.296	0.628	0	0.641
22/04/2010	10.8	1.35	42.46	0.102	0.15	2.022	0	0.32
15/07/2010	11.8	0.22	233.86	8.16	0.48	1.8	0.01	0.257
18/08/2010	2.4	0.43	62.04	0.272	0.34	0.456	0	0.513
19/08/2010	4.83	0.38	57.2	0.136		0.525	0	0.513
26/04/2011	23.2	0.39	51.7	1.36	0.42	1.1061	0.199	0.325
24/11/2011		42.54	79.86	0.204		0	0	0
20/01/2013			47.995	0.34	8.148			
28/04/2013	6.7		75.16	1.36	1.345			
21/07/2013	8.4		187.57		1.216			
14/12/2013		1.275	77.22	0.34	1.65	3.144	0	6.585
19/01/2014		13.5561	77.88	0.068		0.024	0	2.481
19/04/2014		16.963	75.56	0.272	3.425	1.166	0	8.672
22/07/2014			160.3	5.26				
25/09/2014			68.2	0.03				
22/07/2014			168.18	17.884	0.975			
25/09/2014			71.88	0.102				
24/07/2017	2.4	0.13	64.9	0.17				
02/02/2018	9.1	0.3	64.9	1.36		0.03	0	10.36
19/07/2018			126.6	0.34			0	0.0836
28/08/2019	9.5	0.474	86.9	0.34				
17/06/2020	9.6	16.89	39.6	5.96	1.581	0.609	3.29	
30/07/2020		1.03	50.6	0.272	2.612	0.159	0.019	0.335
26/10/2020		0.984	114.4	17.816	1.703	0.3161	0.004	5.515
22/12/2020			147.4	16.32				
23/12/2020			74.8	2.992				

Appendix 8: Box plots showing statistical distribution of fumarole gas discharge data at OMF8



Appendix 9: ENVI-IDL code for selection of hour of day TIR images (Written by Harald van derwerff)

```
; MODIFICATION HISTORY:
;   Written   :   vdwerff, UT-ITC, Jan 2020
;-

pro hw_flirt_import, ev

    compile_opt idl2

    catch, theerror
    if theerror ne 0 then begin
        catch, /cancel
        print, !error_state.msg
        return
    endif

    ; select input files
    files = dialog_pickfile(/read,/multiple_files,filter='*.tif')
    if files[0] eq '' then return
    files = files[sort(files)]

    ; select output file
    bsqfile =
dialog_pickfile(/write,/overwrite_prompt,filter=['*.dat','*.bsq','*'])
    if bsqfile eq '' then return
    hdrfile = bsqfile+'.hdr'

    ; open output file
    openw, lun, bsqfile, /get_lun

    ; query and read tiffs, write each to the output file
    bnames = ''

    for i = 0, n_elements(files)-1 do begin

        ok = query_tiff(files[i],s)

        if (ok) then begin

            bnames = [bnames, file_basename(files[i],'.tif')]

            band = read_tiff(files[i])
            writeu, lun, band

        endif

    endfor

    ; close & write output file
    free_lun, lun

    ; check that any bands have been added
    if n_elements(bnames) eq 1 then return

    ; prepare output file header data
    bnames = bnames[1:*]
    nb = n_elements(bnames)
    ns = s.dimensions[0]
```

```

nl = s.dimensions[1]

; check which datatype we have
datatype = size(band,/type)

; write output file header
openw,lun,hdrfile,/get_lun

printf,lun,'ENVI'
printf,lun,'description = {FLIRT import}'
printf,lun,'samples = '+strtrim(ns,2)
printf,lun,'lines = '+strtrim(nl,2)
printf,lun,'bands = '+strtrim(nb,2)
printf,lun,'header offset = 0'
printf,lun,'file type = ENVI Standard'
printf,lun,'data type = '+strtrim(datatype,2)
printf,lun,'interleave = bsq'
printf,lun,'byte order = 0'
printf,lun,'wavelength_units = "Index"'
printf,lun,'wavelength = {'
printf,lun, strtrim(indgen(nb-2)+1,2)+','
printf,lun, strtrim(nb,2)+'}'
printf,lun,'band names = {'
for i = 0, nb-2 do printf,lun,bnames[i]+','
printf,lun,bnames[nb-1]+'}'
if datatype eq 12 then begin
  printf,lun,'data gain values = {'
  for i = 0, nb-2 do printf,lun,'0.1,'
  printf,lun,'0.1}'
  printf,lun,'data offset values = {'
  for i = 0, nb-2 do printf,lun,'-273.15,'
  printf,lun,'-273.15}'
endif

free_lun,lun

end

```

Appendix 10: Scatter plot (Tmax (ROI-1) vs Tmax (ROI-4) at 09:00 UTC.

